Article:
Aliakbari, R, Kowsari, E, Naderi, HR et al. (4 more authors) (2022) Si-containing 3D cage-functionalized graphene oxide grafted with Ferrocene for high-performance supercapacitor application: An experimental and theoretical study. Journal of Energy Storage, 50. 104635. p. 104635. ISSN 2352-152X

https://doi.org/10.1016/j.est.2022.104635

Si-containing 3D cage-functionalized Graphene oxide grafted with Ferrocene for high-performance supercapacitor application: an experimental and theoretical study

Raouf Aliakbari [a], Elaheh Kowsari [a]*, Hamid Reza Naderi [b], Saeedeh Sarabadani Tafreshi [a], Seeram Ramakrishna [c]*, Amutha Chinnappan [c], Nora H. de leeuw [d,e]

[a] *Department of Chemistry, AmirKabir University of Technology, No. 424, Hafez Avenue, 1591634311, Tehran, Iran*

[b] *Novin Ebtekar Company, Exclusive Agent of Metrohm-Autolab and Dropsens Companies, Tehran, Iran*

[c] *Department of Mechanical Engineering, Center for Nanofibers and Nanotechnology, National University of Singapore, 119260, Singapore*

[d] *School of Chemistry, Cardiff University, Main Building, Park Place, Cardiff CF10 3AT, United Kingdom*

[e] *School of Chemistry, University of Leeds, Leeds LS2 9JT, United Kingdom*

E-mail addresses: Kowsarie@aut.ac.ir (E. Kowsari), and Seeram@nus.edu.sg (S. Ramakrishna)

Abstract

In this work, graphene oxide sheets were functionalized with Octa(aminopropyl)silsesquioxane. Then, Octa(aminopropyl)silsesquioxane-functionalized graphene oxide (GO-Amine-SSQ) was grafted with Ferrocene through Friedel-Craft reaction. Structural properties of the prepared composite (GO-Amine-SSQ-Fc) were analyzed by XPS, FT-IR, XRD, Raman, SEM, TEM, and BET tests. Results confirmed the successful synthesis and high porosity. Next, the electrochemical properties of GO-Amine-SSQ-Fc were characterized by CV, GCD, and EIS techniques in the 3E system. The GO-Amine-SSQ-Fc electrode showed a specific capacitance of 574 F g^{-1} at 1 A g^{-1}, retention capacitance of 90.1% after 10000 charge-discharge cycles, low resistance, and efficient diffusion of ions. After confirming the excellent electrochemical performance of this electrode, a symmetric supercapacitor system (GO-Amine-SSQ-Fc//GO-Amine-SSQ-Fc) was tested by CV and GCD techniques, to determine practical application of system. GO-Amine-SSQ-Fc//GO-Amine-SSQ-Fc system recorded a specific capacitance of 304 F g^{-1} at 0.5 A g^{-1}, retention capacitance of 92.5% over 10000 charge-discharge cycles, and specific energy of 10.14 Wh Kg^{-1} at a specific power of 500 W Kg^{-1}. Also, the results of computational methodology show that the interaction of SSQ, Fc and GO layer in GO-Amine-SSQ-Fc composite, makes it effective as an electrode material for supercapacitors. This excellent performance, as a result of the unique structure of Amine-SSQ groups and the superior electrochemical behavior of Ferrocene groups, suggests that GO-Amine-SSQ-Fc composite has great potential for energy storage devices.

Keywords

Graphene oxide; Silsesquioxane; Ferrocene; Energy storage device; Supercapacitor

1. Introduction

Today, the development of electrical energy storage devices is vital to the energy generation sectors. Energy storage devices' performance determines the cost and operation of the system [1]. These systems can be classified as chemical, electrochemical, thermal, and mechanical storage [2]. Supercapacitors (SCs) are an energy storage device that has received attention due to high retention capacitance, fast charge-discharge cycles, higher specific energy than conventional capacitors and higher specific power compared to rechargeable batteries. SCs store energy through ion adsorption (electrosorption) mechanism (non-faradaic process), pseudocapacitive process (faradaic mechanism through surface redox reactions), or both (hybrid materials) [3]. The non-faradaic mechanism, which stores energy by forming electric double-layers (EDL), is performed by carbonaceous parts of electrode materials. Devices that operate through the non-faradaic mechanism are electric double-layer capacitors (EDLCs) [4]. Pseudocapacitors are another class of SCs that stores charges through oxidation-reduction reactions [5, 6]. The third class of these devices (hybrid SCs) uses both faradaic and non-faradaic mechanisms [7-9]. Therefore, these devices can be classified into EDLCs, pseudocapacitors, and hybrid capacitors. Another type of

classification of SCs is based on their configuration. Based on the electrode configurations in a SC, these energy storage devices are classified as asymmetric [10, 11], battery-type [12], and symmetric [13] SCs. Electrolytes are another important part of SCs that are classified as ionic liquids [14], organic [15], aqueous [16, 17], gel [18], solid-state [19, 20], eutectic solvents [21, 22], polymers [23], redox electrolyte [24], so on.

Also, SC electrodes can be classified according to the type of storage mechanism [25]. These electrodes generally include Pseudocapacitance materials (metal oxides and metal-containing materials [26-32], conducting polymers [33-35], biopolymers [25], MOFs [36-38], heteroatom-containing and heteroatom-doped materials [39-44], etc.), double-layer capacitance materials (graphene [45, 46], CNT [47-49], graphene nanoribbons [50], etc.), and hybrid materials (composites or materials with both properties) [51]. Hybrid materials significantly impact on future developments, which can show superior characteristics over their pure counterparts. Therefore, extensive researches have been done on hybrid material-based electrodes [52, 53]. Graphene with 2D structure has been employed in energy storage devices in recent years due to its unique electrical properties [54]. Other graphene derivatives, such as graphene oxide (GO) [55], functionalized graphene oxide (fGO) [56], and reduced graphene oxide (rGO) [57-60] have also been used to make hybrid composites in the role of SC electrodes [61, 62]. Silsesquioxanes (SSQs) are other advance materials which employed in systems. SSQs are organic-inorganic compounds that improve the mechanical, chemical, and thermal stability of composites [63]. Also, SSQ-containing composites have high surface area, which increases the active surface in the application of SC electrodes [64]. Another compound employed in preparation of composites is Ferrocene (Fc), due to its unique electrochemical properties. Fc leads to more efficient electron-transfer in the composite, hence known as redox modifier and probe. High stability of redox states, low oxidation potential, and effective electron transfer have made Fc a redox modifier [65, 66].

In this work, for the first time, a composite containing GO, Fc, and SSQ (as the bridge) was synthesized. This structural design, in which SSQ acts as a bridge, increases the surface area and modifies the GO surface. On the other hand, increasing the surface cause the electrode to improve energy storage through the EDL mechanism. Also, composites containing GO and SSQ have been rarely investigated in SC applications. In addition to improving electrochemical performance through the EDL mechanism, electrode performance was also improved through Faradaic reactions by Fc groups to achieve an efficient system. Also, simultaneous use of SSQ groups and Fc groups for the synthesis of composite to measure SC performance has not yet been performed. GO was prepared through the modified Hummer method. Next, the GO surface was functionalized with Amine-SSQ, which led to GO-Amine-SSQ composite. Then, through the Friedel-Crafts reaction, a Fc-containing composite (GO-Amine-SSQ-Fc composite) was synthesized. The preparation of this composite was performed to improve the electrochemical behavior as the SC electrode. Successful synthesis and structural characterization of GO-Amine-SSQ-Fc composite were investigated using X-ray photoelectron spectroscopy (XPS), Fourier-transform infrared (FT-IR), X-ray diffraction (XRD), Raman spectroscopy, scanning electron microscopy (SEM), transmission electron microscopy (TEM), and Brunauer-Emmett-Teller (BET) techniques. Also, the electrochemical behavior of GO-Amine-SSQ-Fc composite was carefully studied and discussed by cyclic voltammetry (CV), galvanostatic charge-discharge (GCD), and

electrochemical impedance spectroscopy (EIS) techniques. Also, electrochemical properties of GO-Amine-SSQ-Fc composite was compared with the GO-Amine-SSQ composite to determine the important role of Fc as a redox-active material. Finally, the Fc-containing composite was tested in a symmetric SC system to determine the device's performance in practical application.

2. Experiments

2.1 Materials

All reagents and solvents used in this study were purchased from Sigma-Aldrich and Merck companies and used without further purification.

2.2 Synthesis and Preparation

Preparation of GO and acylated GO (GOCl): To prepare GO, the modified Hummer's method was used according to this reference: [67]. 2.50 g of graphite powder and 1.25 g of $NaNO_3$ were added to 60 ml of H_2SO_4 solution in a round-bottom flask placed in the ice bath (30 min). Next, 7 g of $KMnO_4$ (as the strong oxidizing agent) was added while stirring the solution slowly, and slow stirring was continued for 12 h. Then 150 ml of distilled water was added to the solution, while the reaction solution's temperature reached 96°C, and stirring continued for another 24 h. Next, 50 ml of H_2O_2 (30%) was slowly added to the flask, while the stirring rate was 300 rpm. Finally, the obtained light black powder was washed several times with H_2O and HCl, then dried in a vacuum oven at 100°C. To synthesis of GOCl, 2 g of synthesized GO was refluxed in $SOCl_2$ (4 h), then the excess $SOCl_2$ was removed. Then, GOCl was filtered and washed repeatedly with 40 ml of CH_2Cl_2. **Fig. 1** shows a schematic of synthesis.

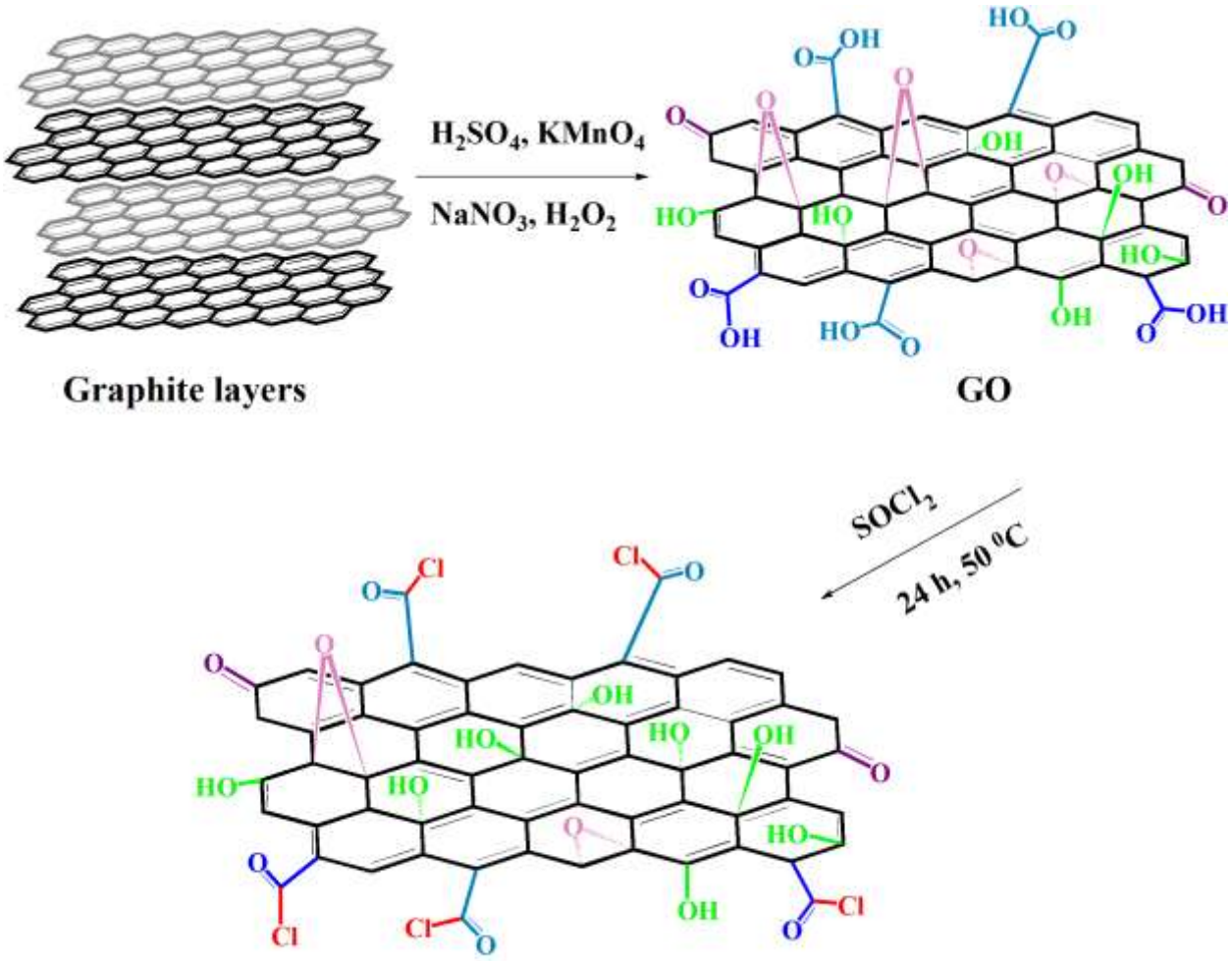

Fig. 1. Preparation of GO and GOCl

Preparation of octa-aminopropyl SSQ (Amine-SSQ): The synthesis of Amine-SSQ was done by a Sol-Gel process according to this reference: [68]. Under N_2 atmosphere, 221.4 g of 3-aminopropyltriethoxysilane was put into a flask equipped with magnetic stirring and reflux cooler. Then 22.5 g of water and 64.9 g of 1-propoxy-2-propanol were added together, then the mixture was added to the flask. Next, the contents of the flask were refluxed at 80°C (45 min). Finally, by vacuum distillation, volatile impurities and solvent were removed (20 mbar, 150°C). A schematic of the three-dimensional Amine-SSQ cage is shown in **Fig. 2**.

Fig. 2. 3D Amine-SSQ cage structure

Preparation of GO-Amine-SSQ composite: First, 2.00 g of synthesized GOCl was dispersed in 50 mL of THF, then reflux was performed for 2 h. Next, 1.00 g of synthesized Amine-SSQ was added to the mixture, and contents of the flask were refluxed for 24 h at 65°C. By filtration, the obtained black powder was washed repeatedly with 40 ml of CH_2Cl_2 and then freeze-dried. Finally, the obtained GO-Amine-SSQ composite was dried again at 25°C and sealed in a bottle. **Fig. 3** shows a schematic of synthesis.

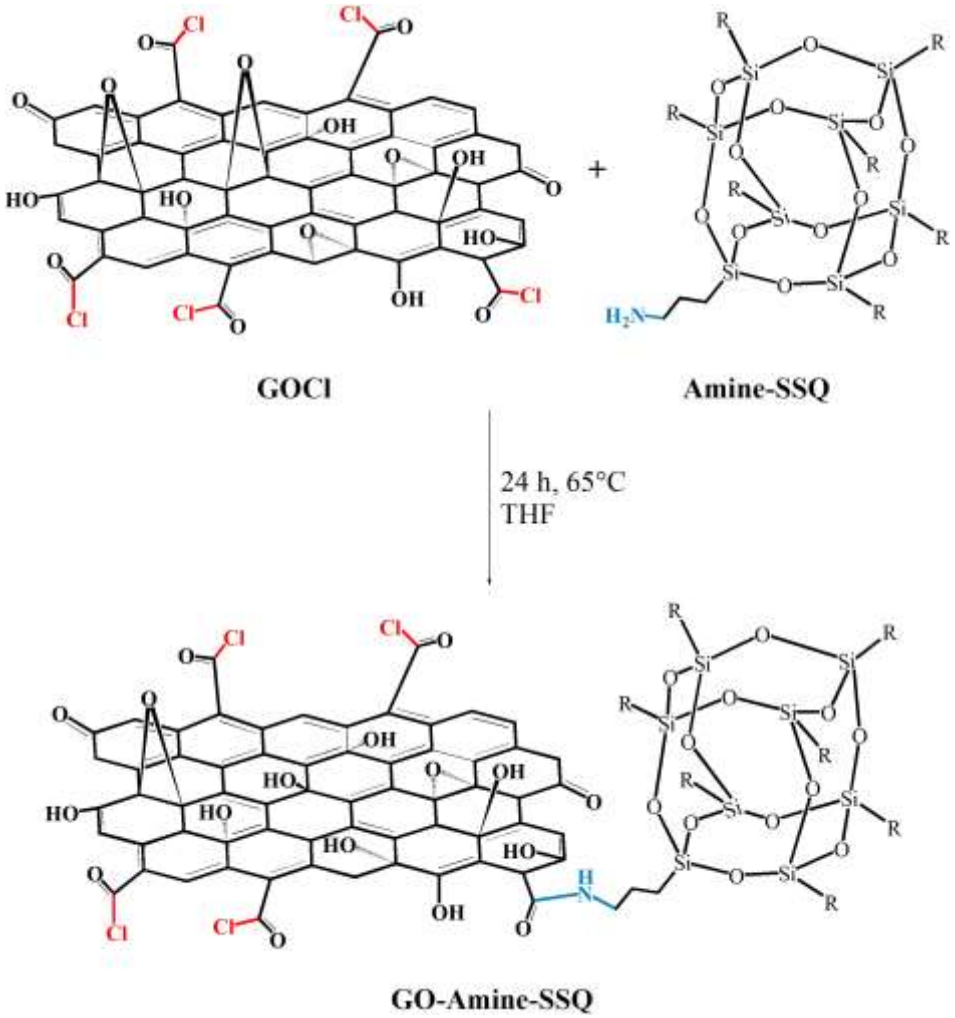

Fig. 3. Preparation of GO-Amine-SSQ composite

Preparation of GO-Amine-SSQ-Fc composite: First, to prepare alkene-functionalized GO-Amine-SSQ, a substitution reaction was used. First, 1.00 g of GO-Amine-SSQ was dissolved in 15 ml of isopropanol, and 0.50 g of NaHCO3 was added to the solution. Then, 10 ml of 3-Chloro-1-propene was added to the synthesis of alkene-functionalized GO-Amine-SSQ. Then, to linking of alkene-functionalized GO-Amine-SSQ and Fc groups, the Friedel-Crafts reaction of alkene-functionalized SSQ (0.50 g) with Fc (0.60 g), in 1,2-dichloroethane (20 ml) at 85°C under stirring for 24 h, was used according to this reference: [69]. A schematic of GO-Amine-SSQ-Fc synthesis is shown in **Fig. 4**.

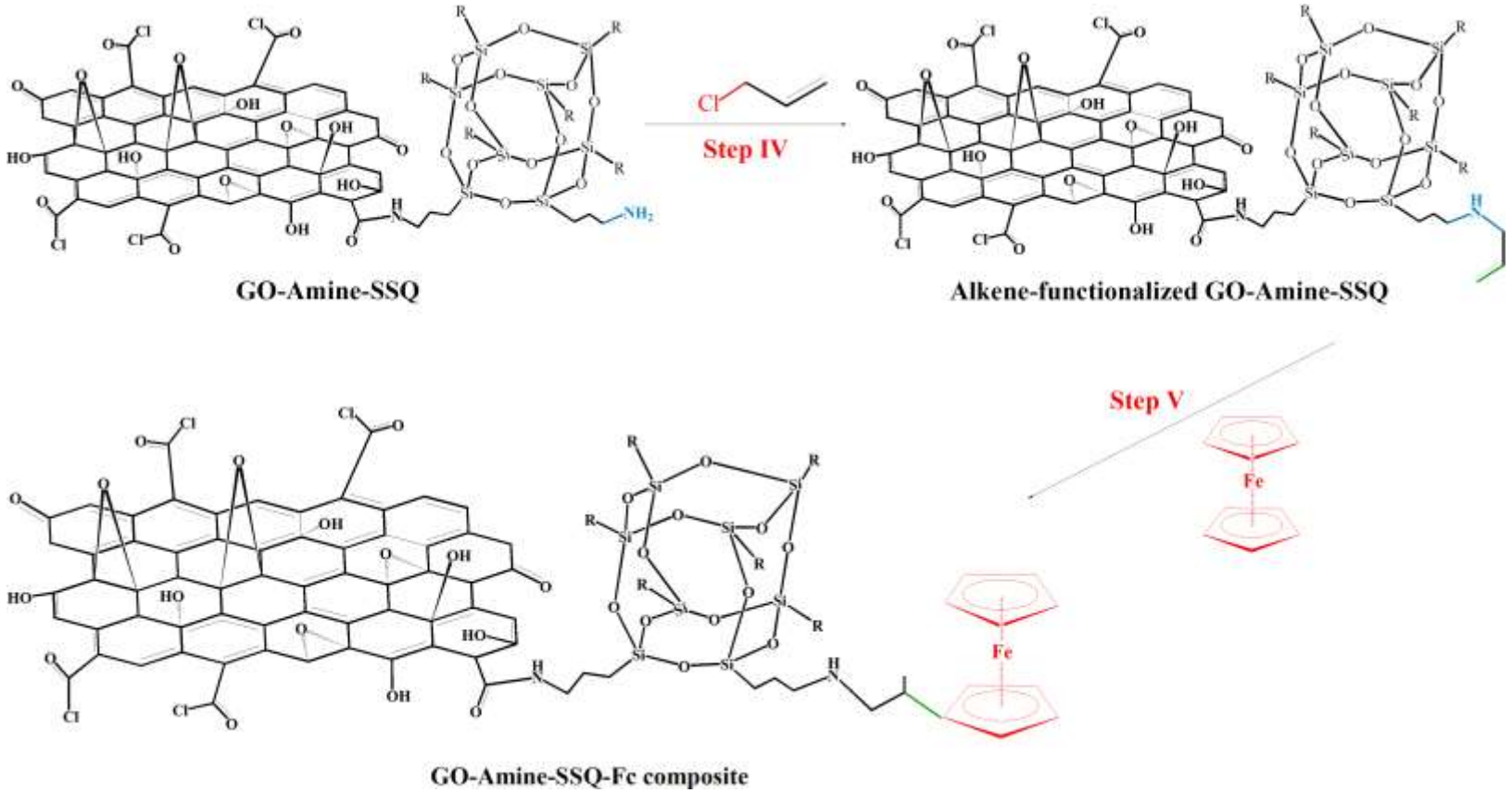

Fig. 4. Synthesis of GO-Amine-SSQ-Fc composite

3. Characterization

3.1 Structural characterization

XPS is a surface analysis technique that can be employed to investigate the surface chemistry of materials [70]. By XPS technique (Kratos Axis Ultra DLD spectrometer (Kratos Analytical Ltd., UK)), the elemental composition, structure, and existing bonds of GO-Amine-SSQ-Fc composite were analyzed. As shown in **Fig. 5a**, the appeared peaks at 98.0, 149.0, 196.0, 280.9, 397.4, 528.0, and 710.4 eV represent Si 2p, Si 2s, Cl 2p, C 1s, N 1s, O 1s, and Fe 2p, respectively. Due to the observed O=C-N bond at 288.1 eV (**Fig. 5b**), grafting between GOCl and Amine-SSQ is performed [71-73]. Also, the binding energies that appeared at 283.7, 284.6, 284.9, 285.7, 285.9, 286.6, 286.9, and 289.09 eV are related to C-Si, C-C / C=C, C-OH, C-Si-O, C-N, C-Cl, C=O, and O=C-O bonds in synthesized functionalized GO, respectively [74, 75]. In the N 1s spectra, grafting was further verified by the N-C=O peak appeared at 398.3 eV (**Fig. 5c**) [76, 77]. Also, **Fig. 5d** represents the high-resolution Si 2p spectrum for GO-Amine-SSQ-Fc composite, which indirectly shows the Si atoms in the SSQ molecule's unique structure (Si-C at 101.7 eV, and Si-O / Si-O-C at 102.7 eV) [78-80]. The appeared peaks at 710.4, and 723.7 eV show Fe $2p_{3/2}$ and Fe $2p_{1/2}$ photoelectron lines, respectively (the iron spectrum (Fe^0) at 705.9 eV shows a characteristic peak), as shown in **Fig. 5e**. Their corresponding satellite (sat.) peaks can be seen at 715.4 and 729.6 eV,

respectively [81-84]. According to the XPS spectra, the synthesis of the GO-Amine-SSQ-Fc composite has been performed successfully.

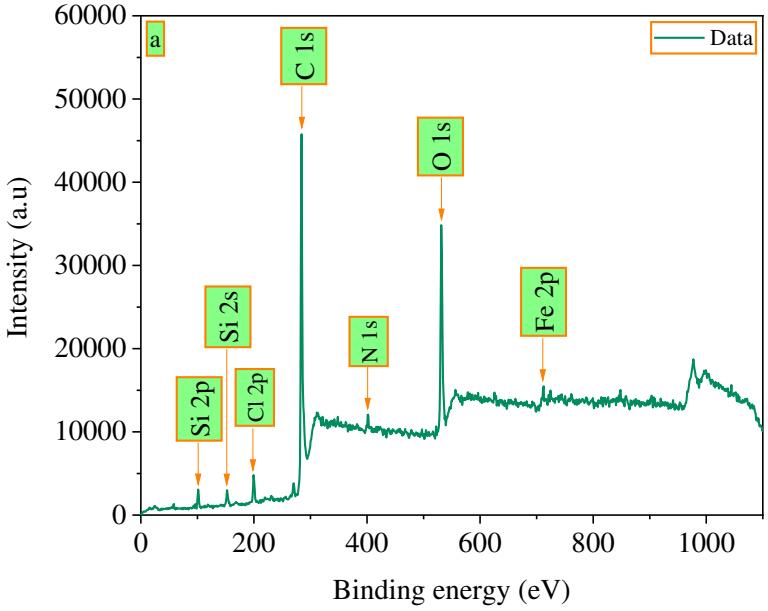

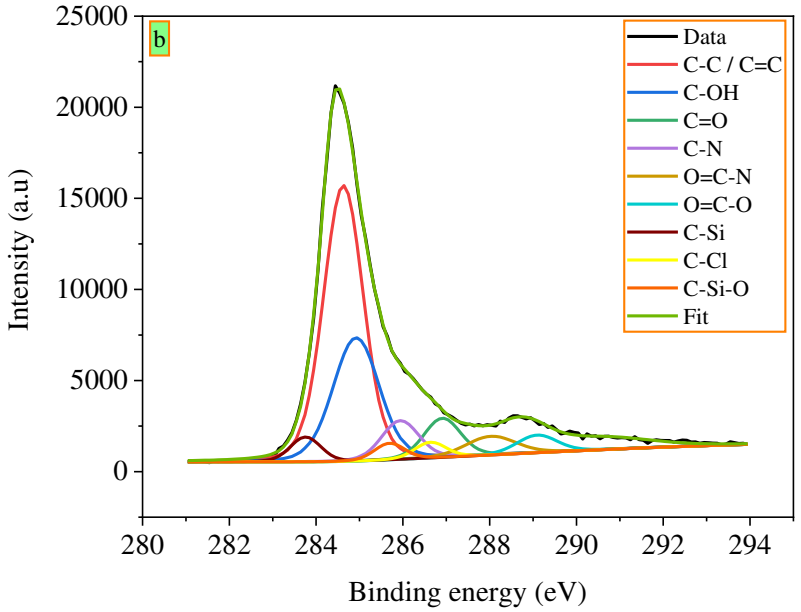

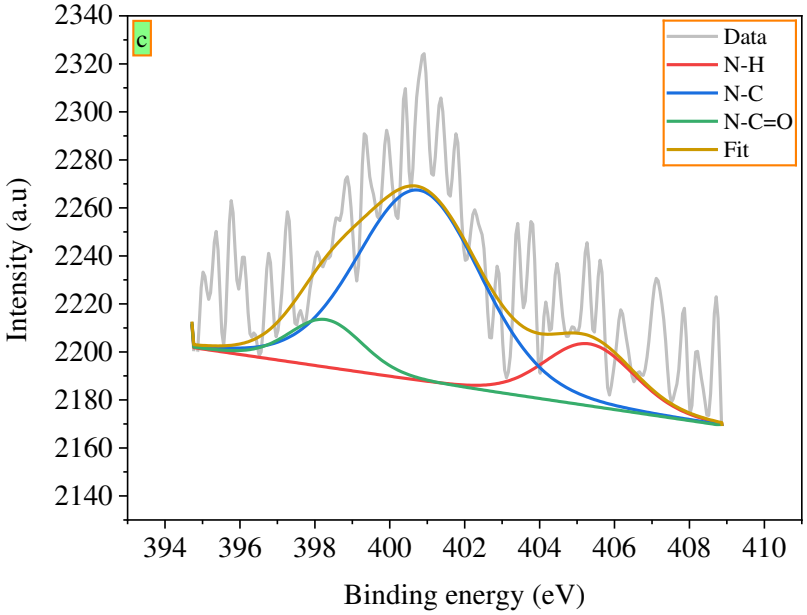

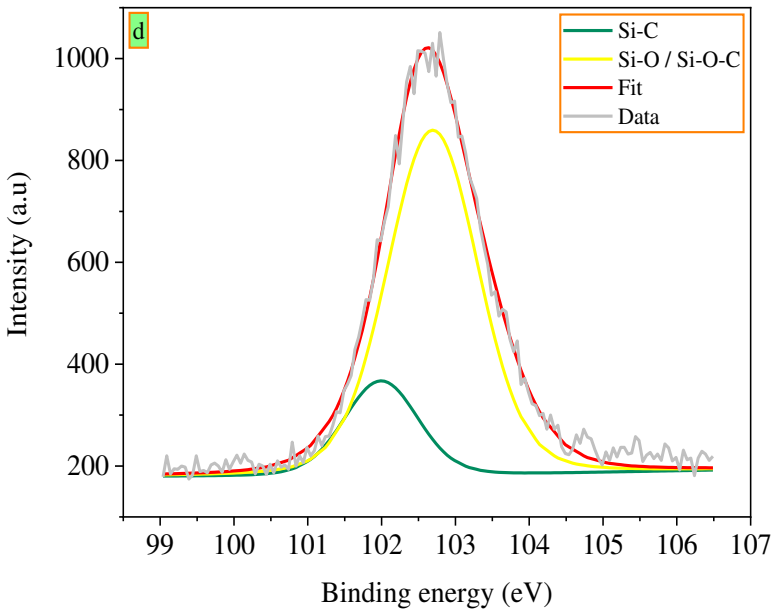

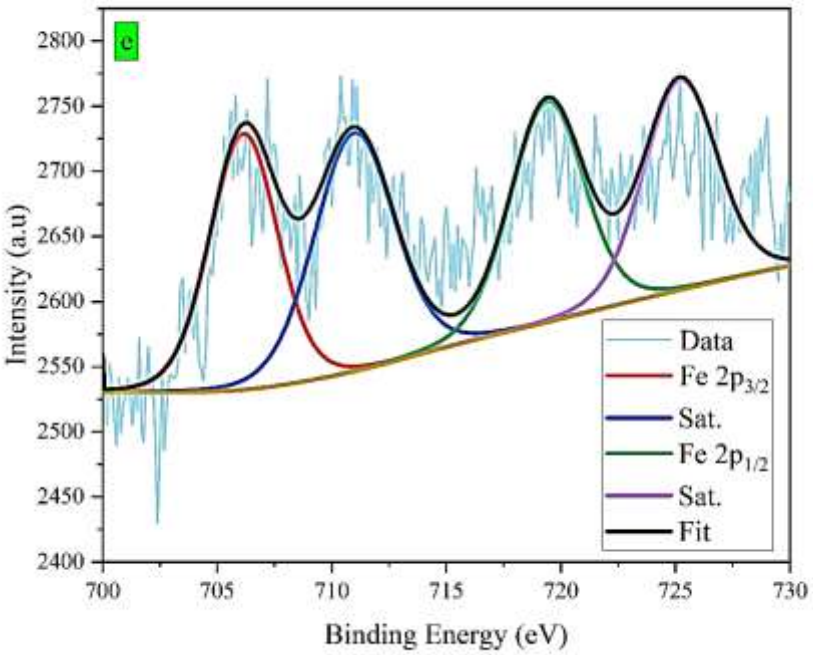

Fig. 5. XPS spectra of GO-Amine-SSQ-Fc composite: **a)** survey spectrum, **b)** C 1s spectrum, **c)** N 1s spectrum, **d)** Si 2p spectrum, and **e)** Fe 2p spectrum

The FT-IR spectrum was recorded with PERKIN-ELMER Spectrum One IR (450-4000 cm^{-1}, KBr pellet). The FT-IR spectrum is shown in **Fig. 6**. Band located at 3430.20 cm^{-1} is attributed to the characteristic transmission of the -NH (stretching). The band that appeared at 1105.62 cm^{-1} is associated with the stretching band of Si-O-Si [82, 85-87]. The bands located at 1573.27, 1410, and 487.46 cm^{-1} were attributed to C=C stretching vibration, bending vibration of saturated C-H bond from cyclopentadienyl rings, and Fe-Cp stretching vibration , respectively, which confirmed the successful Friedel-Crafts reaction between GO-Amine-SSQ and Fc framework without collapse [69, 88-93]. Also, the transmissions at 1718.37cm^{-1}, 1228.29 cm^{-1} as well as 2955.41 and 2872.11 cm^{-1} as well as correspond to the C=O, stretching band of N-C, and C-H stretching, respectively [80, 85, 86, 93, 94].

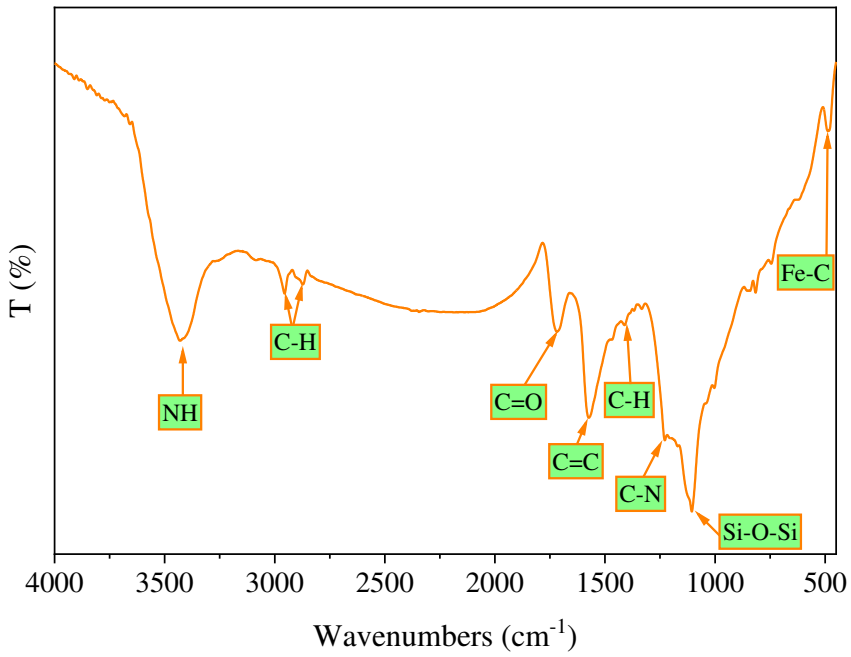

Fig. 6. FT-IR spectrum

The structural properties of GO and GO-Amine-SSQ-Fc composite were further evaluated using XRD as shown in **Fig. 7**. The XRD spectra were recorded by Bruker AXS-D8 advance (10° to 80°, Cu anode, 1.54060 Å). Also, the characteristic peaks of both are listed in **Table 1**. The X-ray spectrum of GO (**Fig. 7a**) shows two characteristic peaks at 2θ= 12.8° (002) and 2θ= 42.5°, which correspond to the interlayer distance of GO sheets and un-exfoliated GO sheets, respectively [95, 96]. The mentioned peaks have shifted to 2θ= 25.7° (002) and 2θ= 42.9° in the GO-Amine-SSQ-Fc composite spectrum (**Fig. 7b**). After the peak shift of 2θ= 12.8° (002) to 2θ= 25.7° (002), the d-spacing is decreased from 0.69 nm to 0.35 nm, because by functionalization of GO, the d-spacing is decreased (cards No. 00-001-0640; 96-901-2233) [97]. Also, the characteristic peak at 2θ= 20.5° correspond to Si-O-Si linkage confirms that SSQ exists without collapsing in the composite structure (cards No. 00-007-0544; 96-705-2732) [98, 99]. Peaks appearing at 2θ= 15.4°, 17.8°, 18.6°, 19.2°, 24.5°, 27.1°, 36.4°, and 41.1° are characteristic peaks of Fc derivatives (cards No. 00-030-1544; 00-044-1740; 96-220-6824) [100-105]. Also, peaks appearing at 2θ= 31.1° and 32.2° can be attributed to H···π interaction and hydrogen bonding [106]. In addition to confirming a porous structure of GO-Amine-SSQ-Fc composite, XRD data guarantees the successful synthesis of this composite.

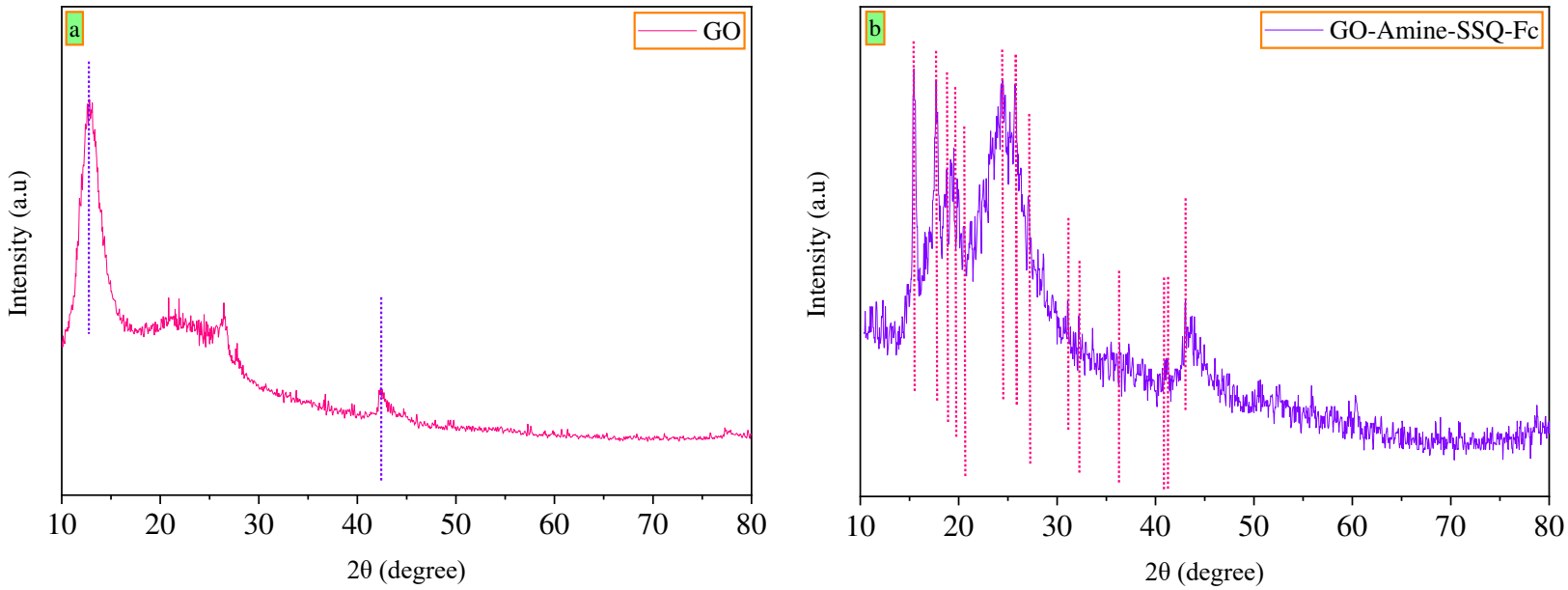

Fig. 7. XRD pattern of **a)** GO, and **b)** GO-Amine-SSQ-Fc composite

Characteristic peaks of	Peak (2θ (degree))	Correspond to	Reference(s)
GO	12.8	Interlayer distance of GO sheets	[95, 96] (Codes: 00-001-0640; 96-901-2233)
	42.5	Un-exfoliated GO sheets	
GO-Amine-SSQ-Fc composite	15.4	Characteristic peaks of Fc derivatives	[100-105] (Codes: 00-030-1544; 00-044-1740; 96-220-6824)
	17.8		
	18.6		
	19.2		
	24.5		
	27.1		
	36.4		
	41.1		
	25.7	Interlayer distance of GO sheets	[95, 96] (Code: 00-001-0640)
	42.9	Un-exfoliated GO sheets	[107] (Code: 96-901-2233)

	20.5	Si-O-Si linkage	[98, 99] (Codes: 00-007-0544; 96-705-2732)
	31.1	H···π interaction and hydrogen bonding	[106]
	32.2		

Table 1. Characteristic peak list of GO and GO-Amine-SSQ-Fc composite

Raman spectroscopy (TakRam N1-541, Teksan Co, 532 nm laser source, 1000-3200 cm^{-1}) was employed to characterize the structural properties of GO and GO-Amine-SSQ-Fc composite. The G and D bands are the two peaks attributed to the sp^2 bonded carbon bonds and the sp^3-defect in the carbon lattice in the Raman spectrum, respectively (robing the nature of defects in graphene by Raman spectroscopy) [108, 109]. As shown in **Fig. 8**, these bands have appeared in the spectrum of both GO (G band at 1578.0 cm^{-1} and D band at 1349.9 cm^{-1}) and GO-Amine-SSQ-Fc composite (G band at 1600.0 cm^{-1} and D band at 1343.5 cm^{-1}). Here, the structural defects of graphene will be investigated by both band intensities described as I_D/I_G ratio. It is clear that I_D/I_G ratio for GO is larger than I_D/I_G ratio for GO-Amine-SSQ-Fc composite, indicating that the sp^3-defects decreased. This phenomenon may be due to the formation of amide bonds and Functionalizing the GO surface.

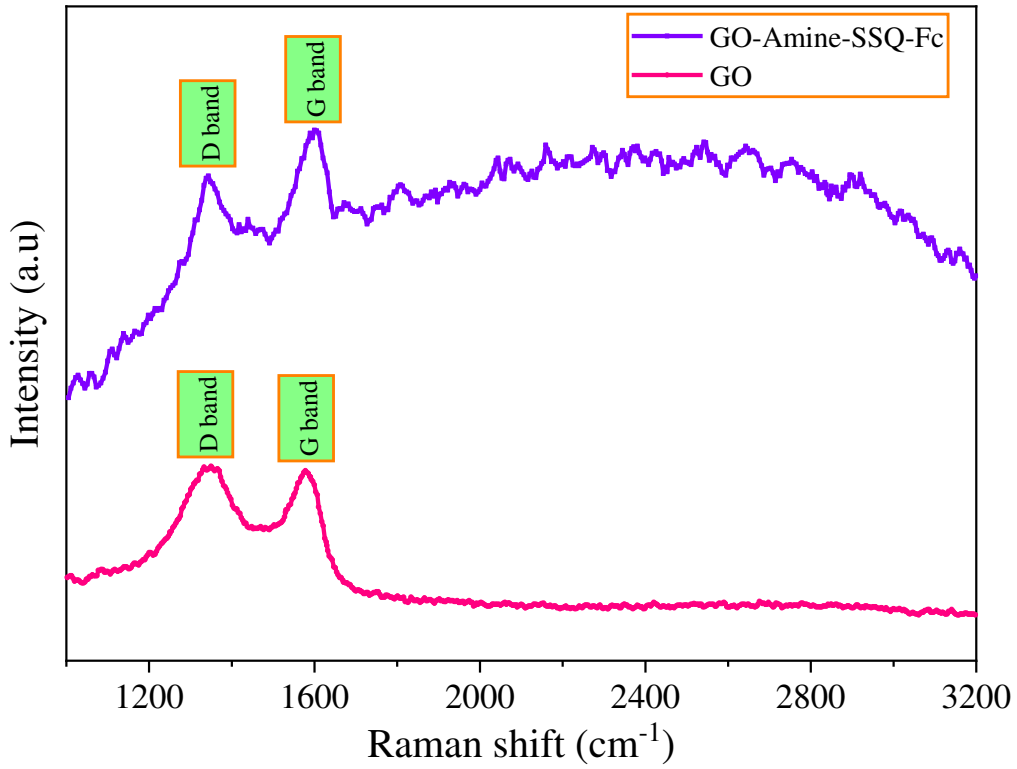

Fig. 8. Raman spectra of GO and GO-Amine-SSQ-Fc composite

SEM (TESCAN Vega3 Model) and TEM (Philips EM208S Model) techniques were applied to accurately analyze the structure, morphology, and microstructural properties of the GO-Amine-SSQ-Fc composite. Due to easy sample preparation and the useful information it provides on sample morphology, SEM is the most utilized technique in the characterization of external morphology (texture) [110]. As can be seen in **Fig. 9**, SEM images clearly show flakes with a large surface area. To further investigate the effect of grafting on the surface morphology of GO, the prepared composite was analyzed using TEM. The TEM images are shown in **Fig. 10**. According to these images, functionalized GO layers show conventional edges with wrinkled and exfoliated and un-exfoliated sheets. Also, SEM and TEM images of GO were added for comparing the morphology of GO and GO-Amine-SSQ-Fc composite. According to **Fig. 11**, GO show conventional edges with exfoliated and un-exfoliated sheets morphology.

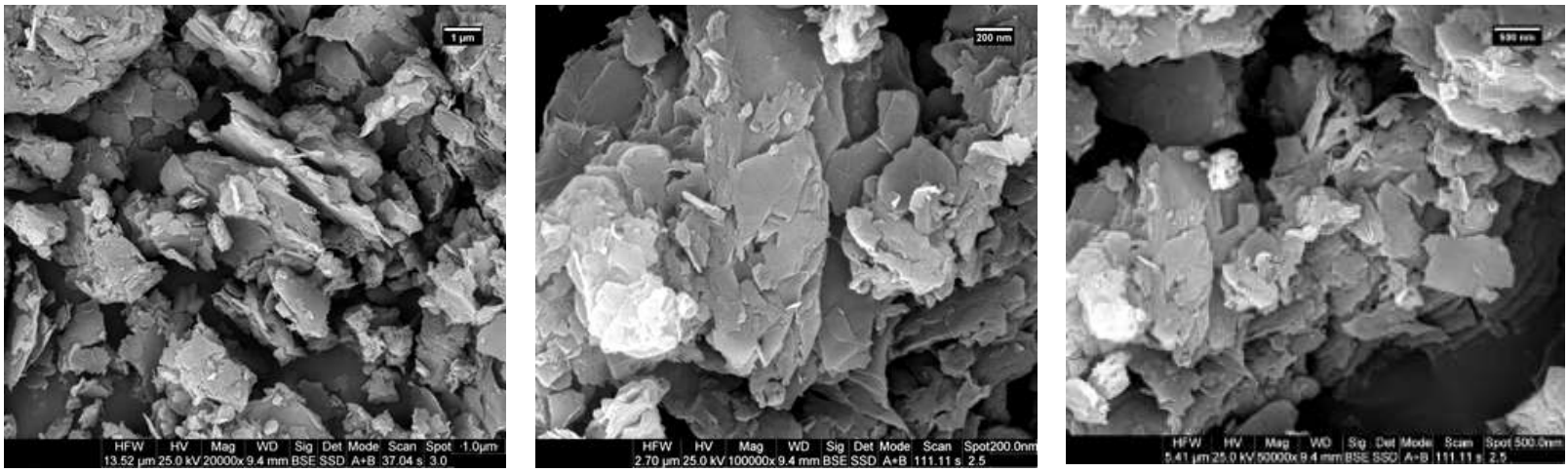

Fig. 9. SEM images of GO-Amine-SSQ-Fc composite with different magnifications

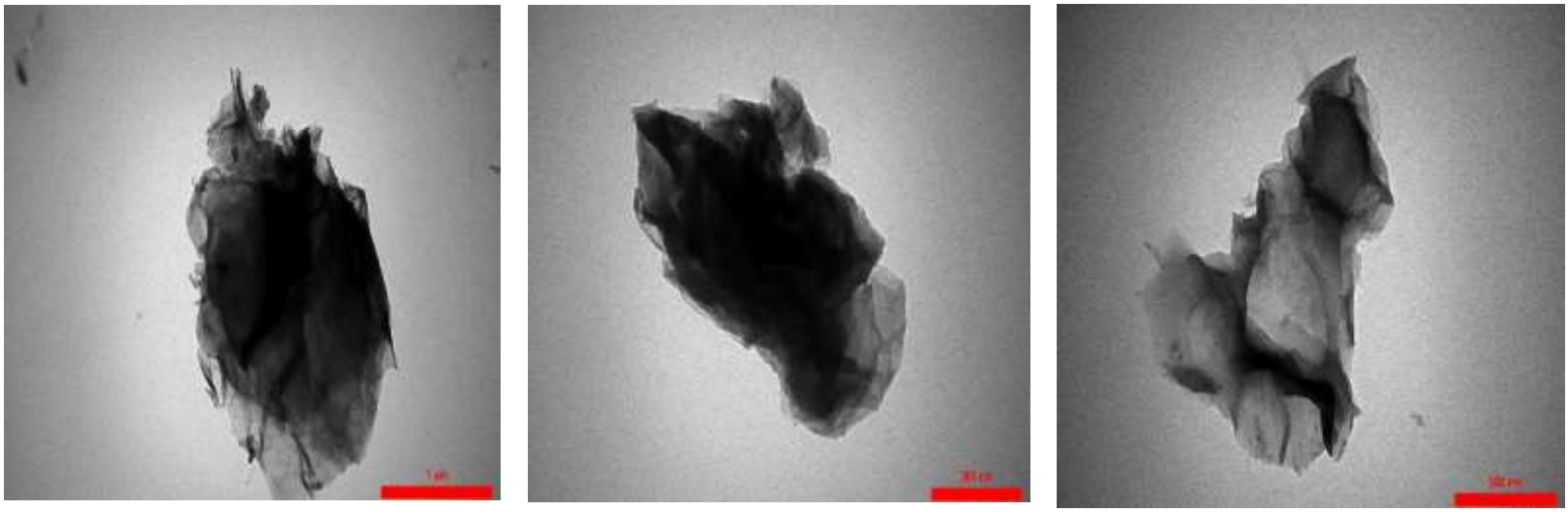

Fig. 10. TEM images of GO-Amine-SSQ-Fc composite

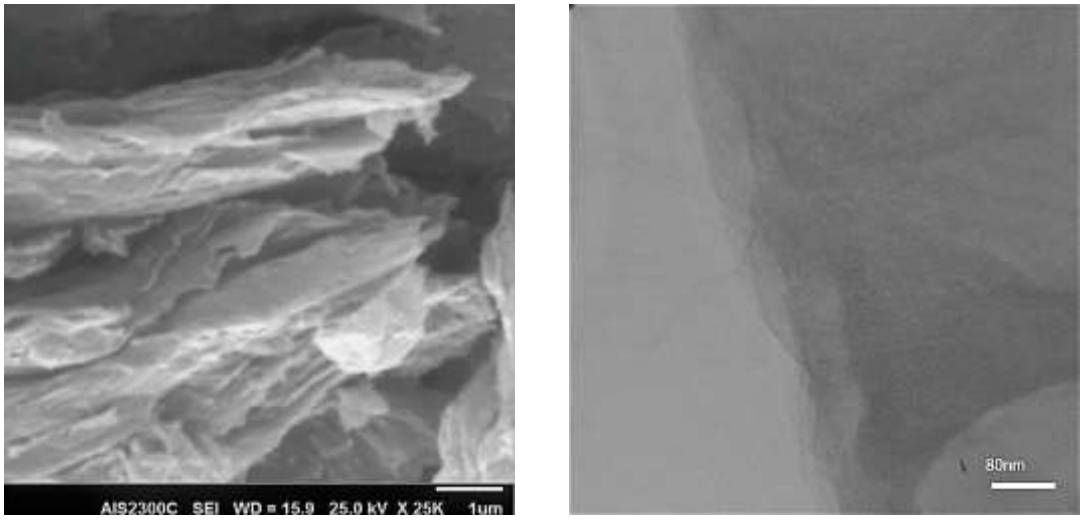

Fig. 11. SEM (right image) and TEM (left image) image of GO

For further morphological investigation (specific surface area, adsorption-desorption behavior, pore-volume, pore diameter, etc.), the GO-Amine-SSQ-Fc composite was analyzed by BET analysis using N_2 sorption measurements at 77 K. The sample was pre-treated before analysis (2h, 120°C). Two devices Finetec and Belsorp mini (JAPAN), were used for analysis. The International Union of Pure and Applied Chemistry (IUPAC) explained N_2 Adsorption Isotherms into six types (I-VI) [111, 112]. According to **Fig. 12a**, the isotherm appears to be of type IV. Given that the desorption curve at $p/p_0 > 6.0$ is almost connected to the adsorption curve, it indicates that the cavities are almost open. The adsorption isotherm remains almost constant in the low and medium

p/p_0 range, which means mono-molecule layer adsorption. Then, at high p/p_0, N_2 adsorption is suddenly increased, indicating the mesoporous nature of the composite [113, 114]. Mesoporous materials are a group of nanoporous materials with a pore size of 2 nm to 50 nm [115] (materials smaller than 2 nm are called microporous, and materials larger than 50 nm are called macroporous [116]). The results of the BET analysis also confirm this behavior. According to these results, the GO-Amine-SSQ-Fc composite's average pore diameter is 11.257 nm. Also, the volume of N_2 adsorbed in monolayer (V_m), total pore volume (at p/p_0= 0.990), and BET surface area ($a_{s\,BET}$) were 30.063 cm^3(STP) g^{-1}, 0.3682 cm^3 g^{-1}, and 130.85 m^2 g^{-1}, respectively. Also, GO was analyzed by BET to determine the influence of surface modification and functionalization. The V_m, total pore volume (at p/p_0= 0.990), and $a_{s\,BET}$ were 7.129 cm^3(STP) g^{-1}, 0.0553 cm^3 g^{-1}, and 31.03 m^2 g^{-1}, respectively. The specific surface area of the GO-Amine-SSQ-Fc composite is 4.2 times larger than that of GO. Also, **Fig. 12b** shows the Barrett-Joyner-Halenda (BJH) plot, which provides useful additional information about the distribution of the pores. According to this diagram, there is a good distribution of pores (from circa 6.9 nm to circa 95.3 nm). Also, the pore volume (V_p) and critical radius ($r_{p,peak}$, the radius of the largest pore that completely filled at any particular pressure [117]) were 0.3195 cm^3 g^{-1} and 53.04 nm, respectively. Unique properties such as meso- and macro- pores and high specific surface area (more active sites) improve electrolyte access and increase specific capacitance due to the synergistic effect of both faradaic (enhanced redox reactions at electrode-electrolyte interfaces) and non-faradaic mechanisms [118-121]. All of these properties make the GO-Amine-SSQ-Fc composite an excellent choice for SC electrodes.

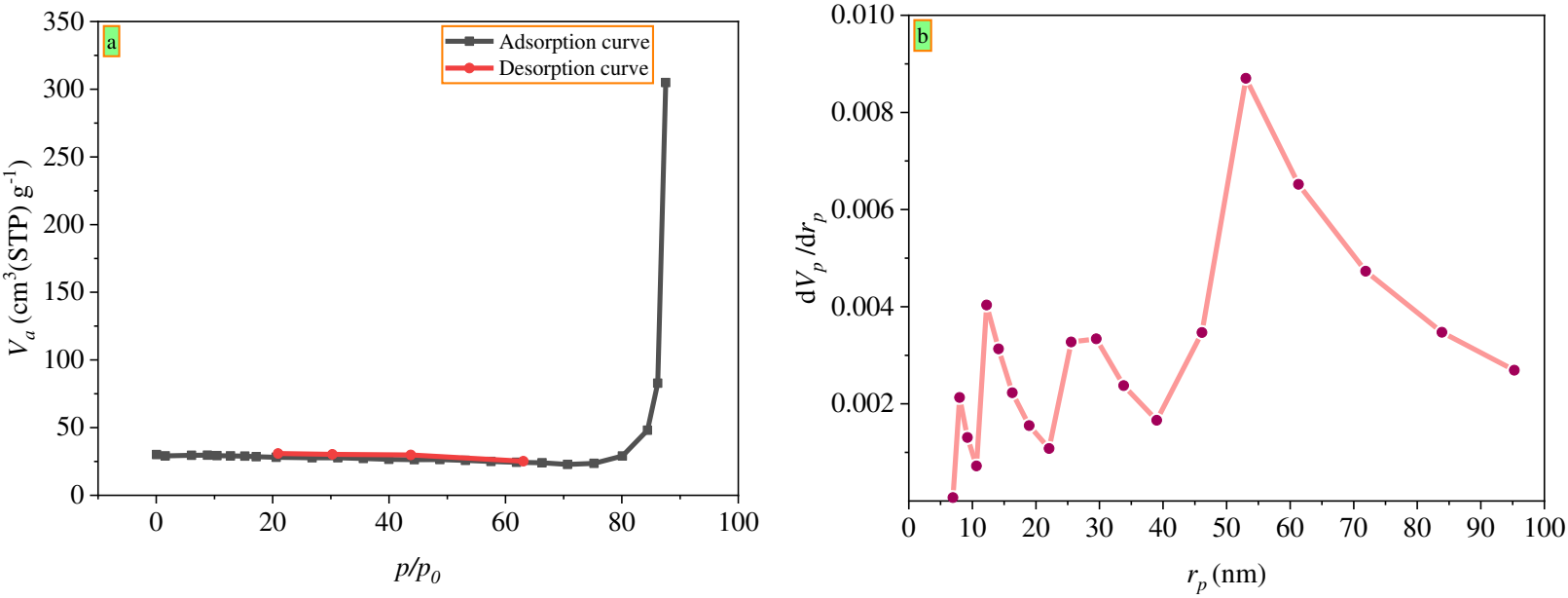

Fig. 12. a) Adsorption/desorption isotherms, and **b)** BJH plot

3.2 Electrochemical characterization

Now that the properties of synthesized composite have been characterized, this section studies and analyzes the electrochemical behavior. All these measurements were performed by Autolab potentiostat PGSTAT 302N (in KCl (3 M) electrolyte, at 25°C). First, the electrochemical properties of the GO-Amine-SSQ composite and GO-Amine-SSQ-Fc composite in a 3-electrode (3E) system are investigated, which electrodes containing composites, Pt sheet, Ag/AgCl (3 M KCl) electrode were used as working electrode, counter-electrode, and reference electrode, respectively. Working electrodes include 70% composite, 15% carbon black, 10% graphite, and 5% PTFE, which were mixed using ethanol and then pressurized on a stainless-steel current collector (1 cm× 1 cm) under a pressure of 10 MPa. After analyzing the two composites by CV, GCD, and EIS tests in the 3E system, the composite that exhibited better electrochemical behavior was examined in the 2-electrode (2E) system by CV and GCD tests as a symmetric SC. For this purpose, a stainless steel cell was utilized where a polypropylene sheet separates positive and negative electrodes. The same method as before was applied to prepare the electrodes.

3.2.1 Electrochemical performance of composites

To determine the electrochemical behavior of the prepared composites, CV was used in a potential window of -0.3 to 0.7 V in the 3E system. The graphs are shown in **Fig. 13a**, which are correlated to the CV results at a scan rate of 50 mV s^{-1}, confirm that the CV loop of GO-Amine-SSQ-Fc composite has a larger surface area and higher current than the GO-Amine-SSQ composite. In addition to having a larger surface area and higher CV current, the shape of loops should also have a lower contact resistance to be introduced as an excellent electrode in SC application. The effect of contact resistance on the diagrams is that the larger resistance contorts the CV pattern, leading to a narrower loop with an oblique angle [122]. To investigate this phenomenon, the two composites' CVs were recorded at a scan rate of 5 to 100 mV s^{-1}, to determine what pattern the graphs of each composite show at low and high scan rates. According to **Fig 13b**, the diagrams recorded in the 3E system, where the electrode containing GO-Amine-SSQ composite performs as the working electrode, show the quasi-rectangular images, corresponding to the both EDL (by carbonaceous parts) and pseudocapacitive behavior (by heteroatom-containing groups) of composite [123, 124]. This pattern is also maintained during increasing scan rates. **Fig. 13c** shows the CV diagrams of GO-Amine-SSQ-Fc composite in the same system. Clearly, composite containing Fc exhibit different electrochemical behavior. In the CV diagrams of GO-Amine-SSQ-Fc composite, the distortion from the rectangular shape originated from the pseudocapacitive behavior of Fc. The Fc/Fc^+ (Ferrocene/Ferrocenium) is a reversible redox pair that enables the system to store energy through faradaic reactions ($(Fe(II)Cp_2 \leftrightharpoons Fe(III)Cp_2 + e^-)$ [125-127]. It can be concluded that the GO-Amine-SSQ-Fc composite, as the hybrid material, stores the charge through both faradaic (by Fc/Fc^+ couple and GO-Amine-SSQ contains heteroatoms groups) and non-faradaic (by carbonaceous parts) mechanisms. Results attest to the synergistic effect between GO-Amine-SSQ and Fc groups.

The energy storage mechanism of GO-Amine-SSQ-Fc composite has led to a significant improvement in energy storage performance. **Fig. 13d** shows specific capacities at various scan rates, which are calculated using this equation [128]: $SC = (\int I.dv)/(V_s.\Delta V.m)$, where SC, $\int I.dv$, V_s,

ΔV, and m are specific capacity, integral area under the CV diagram, scan rate, applied potential window, and active material's mass loading, respectively. The specific capacities of GO-Amine-SSQ composite at different scan rates are as follows: 377 F g^{-1} at 5 mV s^{-1}; 325 F g^{-1} at 10 mV s^{-1}; 284 F g^{-1} at 20 mV s^{-1}; 253 F g^{-1} at 30 mV s^{-1}; 231 F g^{-1} at 40 mV s^{-1}; 211 F g^{-1} at 50 mV s^{-1}; 181 F g^{-1} at 75 mV s^{-1}; 164 F g^{-1} at 100 mV s^{-1}; 131 F g^{-1} at 200 mV s^{-1}. Also, the specific capacities of GO-Amine-SSQ-Fc composite at various scan rates are as follows: 598 F g^{-1} at 5 mV s^{-1}; 545 F g^{-1} at 10 mV s^{-1}; 499 F g^{-1} at 20 mV s^{-1}; 461 F g^{-1} at 30 mV s^{-1}; 429 F g^{-1} at 40 mV s^{-1}; 399 F g^{-1} at 50 mV s^{-1}; 348 F g^{-1} at 75 mV s^{-1}; 323 F g^{-1} at 100 mV s^{-1}; 284 F g^{-1} at 200 mV s^{-1}. With increasing scan rates, the specific capacities of both composites have decreased. The reduction of specific capacities can be interpreted as reducing the effective electrode/electrolyte interaction at high scan rates [129, 130]. Interestingly, while increasing the scan rate from 5 to 200 mV s^{-1}, the specific capacities of GO-Amine-SSQ composite and GO-Amine-SSQ-Fc composite are decreased by 65.3% and 52.5%, respectively. The improved capacitive performance of GO-Amine-SSQ-Fc composite compared to GO-Amine-SSQ composite can be attributed to the less mass transport resistance and the more efficient electrode/electrolyte interaction [75, 131].

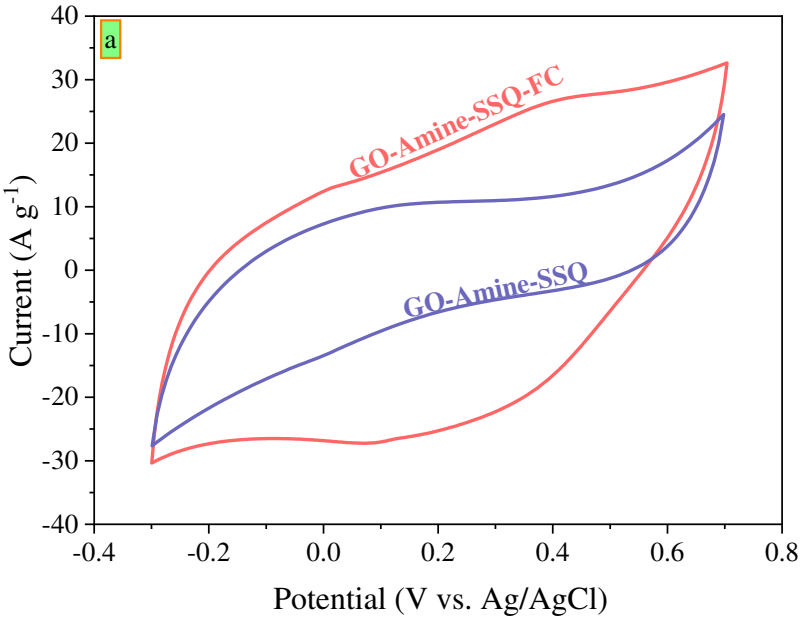

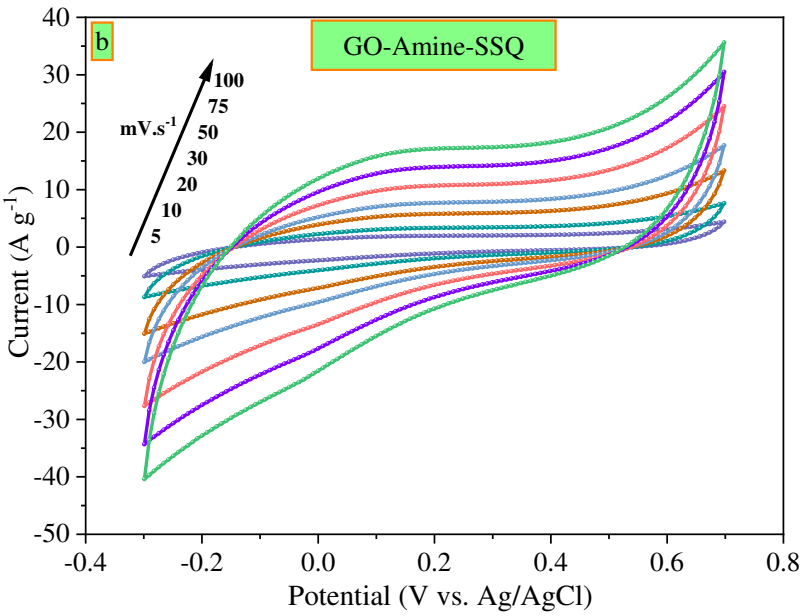

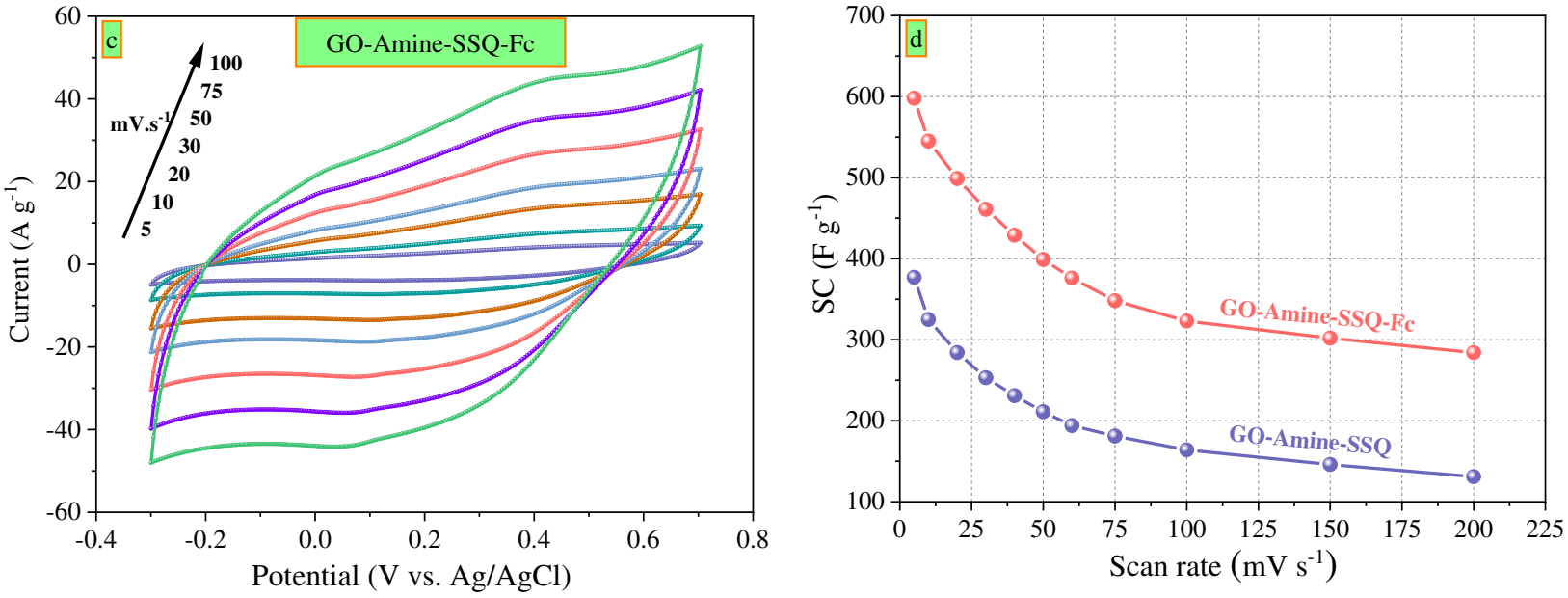

Fig. 13. a) CV diagram of GO-Amine-SSQ composite vs. CV diagram of GO-Amine-SSQ-Fc composite at scan rate of 50 mV s^{-1}, **b)** CV diagrams of GO-Amine-SSQ composite at scan rates of 5 to 100 mV s^{-1}, **c)** CV diagrams of GO-Amine-SSQ-Fc composite at scan rates of 5 to 100 mV s^{-1}, and **d)** Calculated specific capacities at various scan rates (5 to 200 mV s^{-1})

GCD technique was applied to more investigate the electrochemical properties and storage performance as well as practical applicability of the two composites. All measurements were performed in the potential window of -0.3 to 0.7 V in the 3E system. **Fig. 14a** presents the charge-discharge diagrams of both composites at a current density of 2 A g^{-1} in one frame. The slope deviation of graphs from the symmetrical triangular shape confirms that both composites simultaneously benefit from faradaic and non-faradaic mechanisms, which confirms the CV results [132-134]. One of the parameters that is considered to evaluate the performance of an electrode is the discharge time in the charge-discharge diagram, which directly affects the specific capacity, according to this equation [135]: $SC = (I.\Delta t)/(m.\Delta V)$, where SC, I, Δt, m, and ΔV are specific capacity, charge-discharge current, discharge time, active material's mass loading, and applied potential window, respectively. The discharge times of GO-Amine-SSQ composite and GO-Amine-SSQ-Fc composite at the current density of 2 A g^{-1} are 176 and 280 s, respectively, which confirms the significantly higher discharge time of GO-Amine-SSQ-Fc composite (59.1% higher discharge time) compared to the GO-Amine-SSQ composite. The results once again confirm the synergistic effect of the compounds in Fc-containing composite in the application of SC electrode.

Also, GDC tests were recorded at different current densities to study the electrochemical behavior of both electrodes at different current densities and the calculation of specific capacities using discharge times. **Fig. 14b** and **Fig. 14c** show the charge-discharge plots of GO-Amine-SSQ composite and GO-Amine-SSQ-Fc composite, respectively (at the current densities of 1 to 16 A g^{-1}). As the current densities increase, the charging and discharging times decrease, owing to the limited accessibility of electrolyte ions [136]. The specific capacities of two composites at current

densities of 1 to 32 A g^{-1} are shown in **Fig. 14d**, which is calculated using the equation described in the previous paragraph (SC = (I.Δt)/(m.ΔV)). The specific capacities of GO-Amine-SSQ composite at various current densities are as follows: 363 F g^{-1} at 1 A g^{-1}; 352 F g^{-1} at 2 A g^{-1}; 332 F g^{-1} at 4 A g^{-1}; 288 F g^{-1} at 8 A g^{-1}; 240 F g^{-1} at 16 A g^{-1}; 160 F g^{-1} at 32 A g^{-1}. Also, the specific capacities of GO-Amine-SSQ-Fc composite at various current densities are as follows: 574 F g^{-1} at 1 A g^{-1}; 560 F g^{-1} at 2 A g^{-1}; 540 F g^{-1} at 4 A g^{-1}; 488 F g^{-1} at 8 A g^{-1}; 416 F g^{-1} at 16 A g^{-1}; 320 F g^{-1} at 32 A g^{-1}. The specific capacities of Fc-containing composite are significantly higher so that at a current density of 32 A g^{-1}, its specific capacity is two times higher than GO-Amine-SSQ composite. Also, while increasing the current density from 1 to 32 A g-1, GO-Amine-SSQ composite and GO-Amine-SSQ-Fc composite retained 44.1% and 55.7% of initial specific capacitance, respectively, which agrees with the CV results. The improved electrochemical behavior of GO-Amine-SSQ-Fc composite than GO-Amine-SSQ composite can be explained as that after the interaction of GO-Amine-SSQ groups and Fc groups, the diffusion path for accessibility of electrolyte ions is shortened, and charge transfer is facilitated [137, 138].

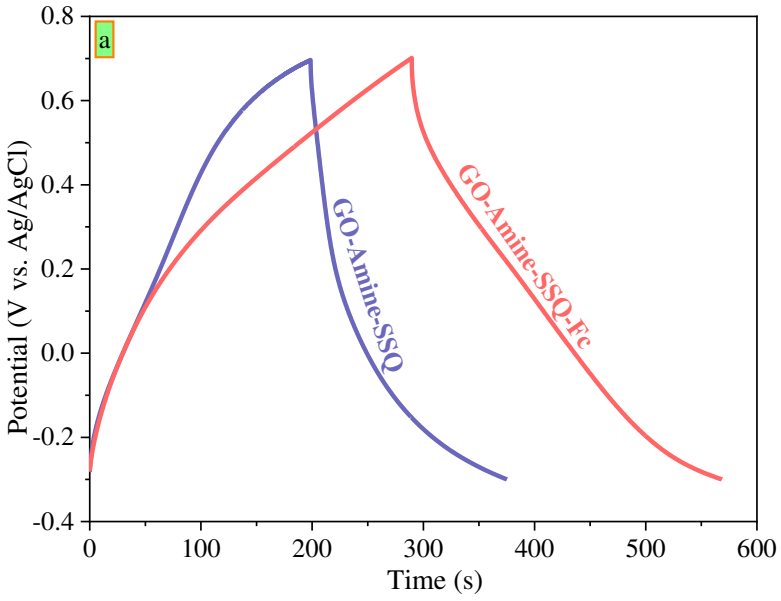

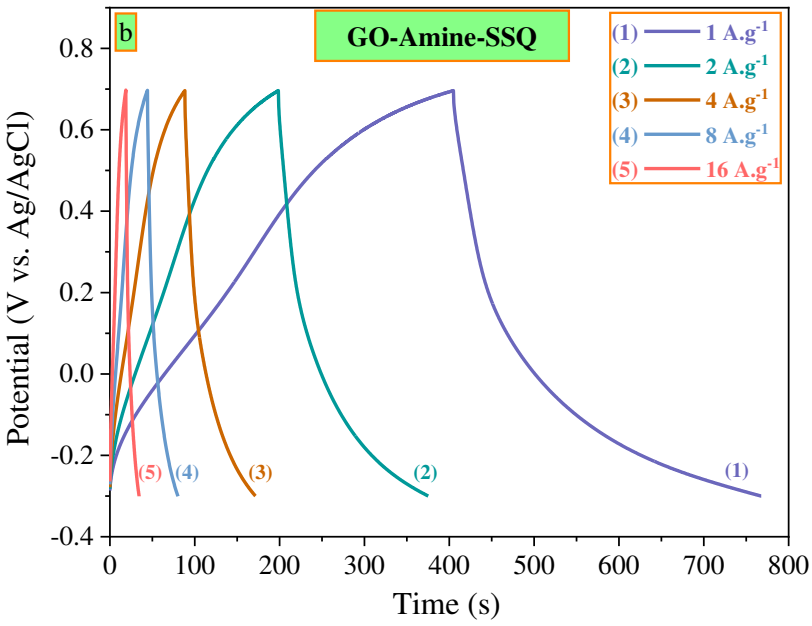

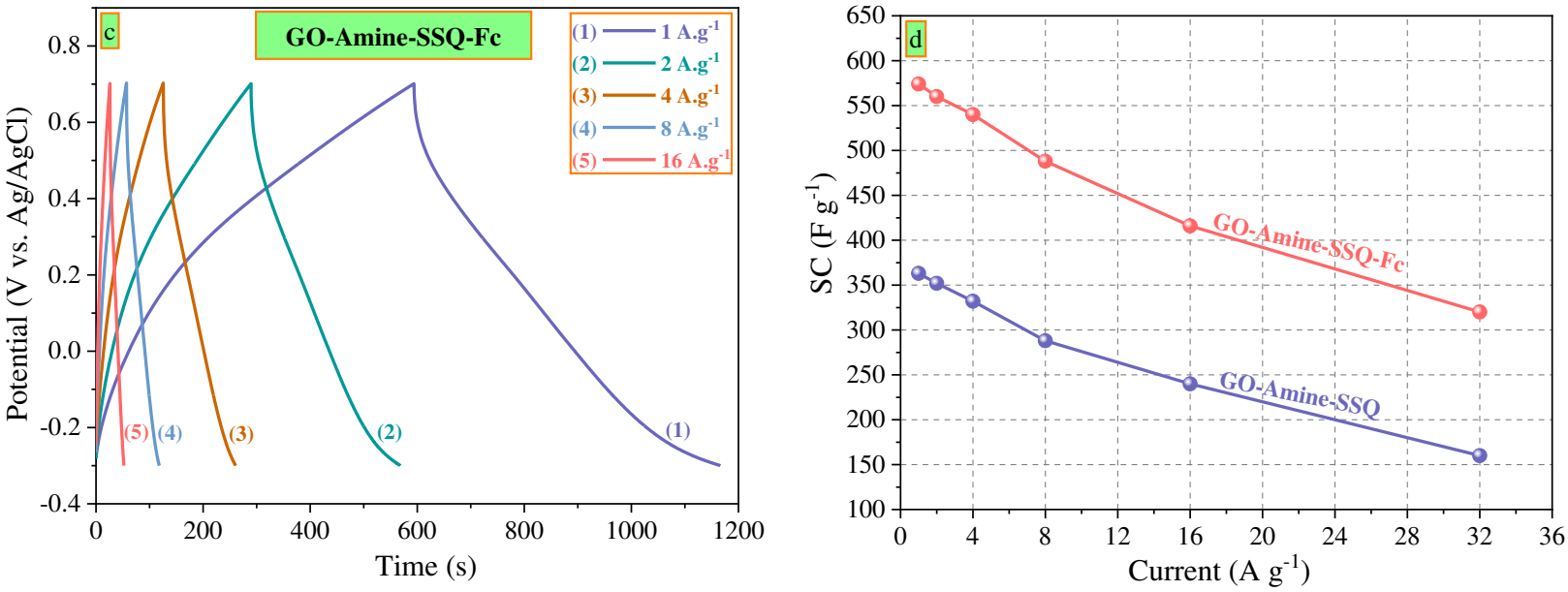

Fig. 14. a) GCD diagram of GO-Amine-SSQ composite vs. GCD diagram of GO-Amine-SSQ-Fc composite at a current density of 2 A g^{-1}, **b)** GCD diagrams of GO-Amine-SSQ composite at current densities of 1 to 16 A g^{-1}, **c)** CV diagrams of GO-Amine-SSQ-Fc composite at current densities of 1 to 16 A g^{-1}, and **d)** Calculated specific capacities at various current densities (1 to 32 A g^{-1})

Also, the stability of both composites during successive charge-discharge cycles was analyzed. As shown in **Fig. 15**, GO-Amine-SSQ composite and GO-Amine-SSQ-Fc composite retained 94% and 90.1% of initial specific capacitance after 10000 charge-discharge cycles at a current density of 16 A g^{-1}, respectively. Although the faradaic reactions can improve the pseudocapacitive behavior of active materials, these reactions cause the electrodes to be destroyed during successive charge-discharge cycles [3]. However, both electrodes granted good retention capacities and high stability for practical applicability.

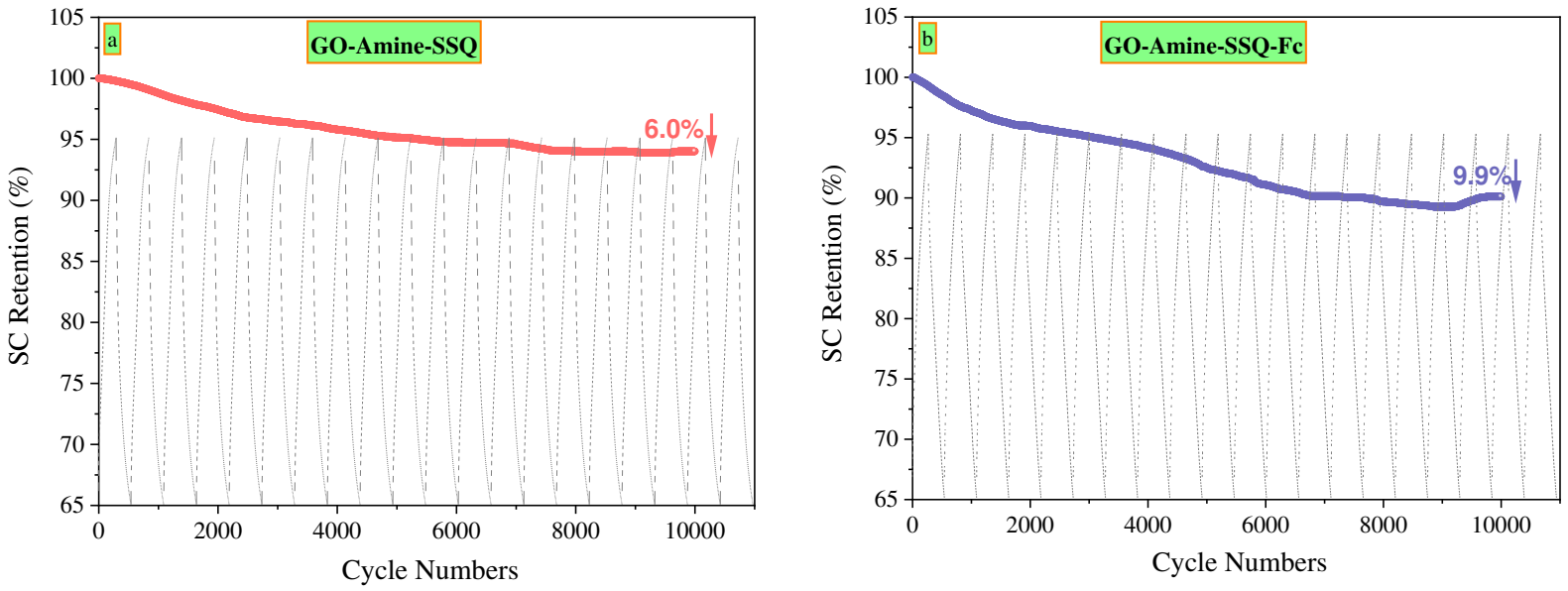

Fig. 15. Retention capacitance of **a)** GO-Amine-SSQ composite, and **b)** GO-Amine-SSQ-Fc composite

The EIS test was deployed for a deeper understanding of the behavior and properties of active material in a system and to conclude its performance as the SC electrode. By EIS technique, charge transfer, ion diffusion, and capacitance behavior at the electrode and electrolyte interface were analyzed. The results of this test are shown in **Fig. 16** as a plot called Nyquist (100 kHz to 0.01 Hz). According to Nyquist plots, a smaller semicircle at the high-frequency regions indicates lower charge transfer resistance (R_{ct}) of the Fc-containing composite. Also, the more inclined the linear region of the Nyquist plot (Warburg diffusion element (Z_w)) in low-frequency areas to the vertical line confirms the efficient diffusion path, which agrees with the more efficient diffusion path of the GO-Amine-SSQ-Fc composite [73, 139]. The extracted data after fitting are also studied (**Table 2**). Fc-containing composite shows lower bulk solution resistance (R_s) and R_{ct} than GO-Amine-SSQ composite. Also, value of Z_w for GO-Amine-SSQ-Fc composite is around two times more than GO-Amine-SSQ composite, confirming more efficient diffusion of ions. Energy storage efficiency through non-faradaic (Q_1) and faradaic (C_F) mechanisms is also shown in **Table 2**. Clearly, the energy storage performance of the GO-Amine-SSQ-Fc composite is much better than the GO-Amine-SSQ composite through both mechanisms.

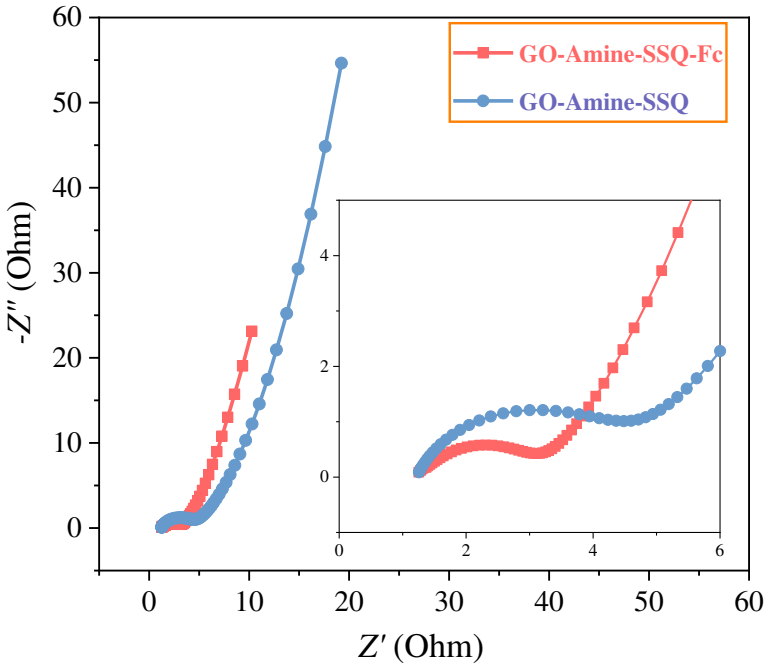

Fig. 16. The Nyquist plots (100 kHz to 0.01 Hz)

Composite	R_s (Ω)	R_{ct} (Ω)	Z_w	Q_1 (mF)	C_F (mF)
GO-Amine-SSQ composite	1.22	3.30	0.06	0.41E-3	0.04
GO-Amine-SSQ-Fc composite	1.20	1.90	0.13	0.75E-3	0.10

Table 2. The extracted data after fitting

As a brief conclusion, both composites have excellent electrochemical behavior as SC electrodes. However, the Fc-containing electrode has better electrochemical properties, making it suitable for application in a 2E system. Also, the electrochemical properties of the GO-Amine-SSQ-Fc composite were compared to electrodes containing similar components. The compared data can be seen in **Table 3**.

Active material	Specific capacitance	Retention capacitance	Reference
Fc-MWCNTs (containing MWCNT and Fc)	50 F g^{-1} at 0.25 A g^{-1}	90.8% after 5000 cycles	[140]

FcGA (containing polyaniline, graphene, and Fc)	960 F g^{-1} at 1 A g^{-1} ~500 F g^{-1} at 3 A g^{-1}	86% after 5000 cycles	[137]
GQD-Fc/PPy (containing polypyrrole, graphene, and Fc)	284.01 F g^{-1} at 2.5 A g^{-1}	86% after 5000 cycles	[141]
GO-PolyFc (containing GO and Fc)	200 F g^{-1} at 1 A g^{-1}	96% after 2000 cycles	[124]
Ferrocene modified GO (containing GO and Fc)	127 F g^{-1} at 1 A g^{-1}	93% after 5000 cycles	[142]
GO-Amine-SSQ-Fc (containing GO, SSQ, and Fc)	574 F g^{-1} at 1 A g^{-1} ~555 F g^{-1} at 2.5 A g^{-1} ~550 F g^{-1} at 3 A g^{-1}	90.1% after 10000 cycles	This work

Table 3. Electrochemical properties of Fc-containing composites in the 3E system

By comparing the electrochemical properties of the composites listed in **Table 3**, the design of SSQ-functionalized GO and its grafting to sandwiched Fc has significantly improved the electrochemical behavior. What is being compared here is electrochemical performance, along with cyclic stability. The system with high cyclic stability maintains its efficiency during successive charge-discharge cycles and generates less electronic waste, which causes less damage to the environment [143, 144]. Specifically, the GO-Amine-SSQ-Fc composite shows high stability compared to the composites listed in **Table 3** (except Ferrocene modified GO composite). The stability of Ferrocene modified GO composite is slightly higher than that of GO-Amine-SSQ-Fc composite, however, its specific capacitance is 4.5 times less than that of GO-Amine-SSQ-Fc composite [142]. Also, one of the unique properties of SCs is the quick charge and discharge, which enables the system to show acceptable electrochemical performance at high charge-discharge current densities. In terms of specific capacitance, FcGA composite [137] and GQD-Fc/PPy composite [141] are competitors of the GO-Amine-SSQ-Fc composite. At high current densities, GO-Amine-SSQ-Fc composite has superior electrochemical performance; this composite also has higher cyclic stability than the two composites FcGA and GQD-Fc/PPy. Superior electrochemical performance of GO-Amine-SSQ-Fc composite can be thanks to increasing the active surface area in the presence of SSQ groups, reducing the composite resistance, more efficient diffusion path, so on. **Fig. 17** provides a simple schematic of the design of GO-Amine-SSQ-Fc composite and the results of this design.

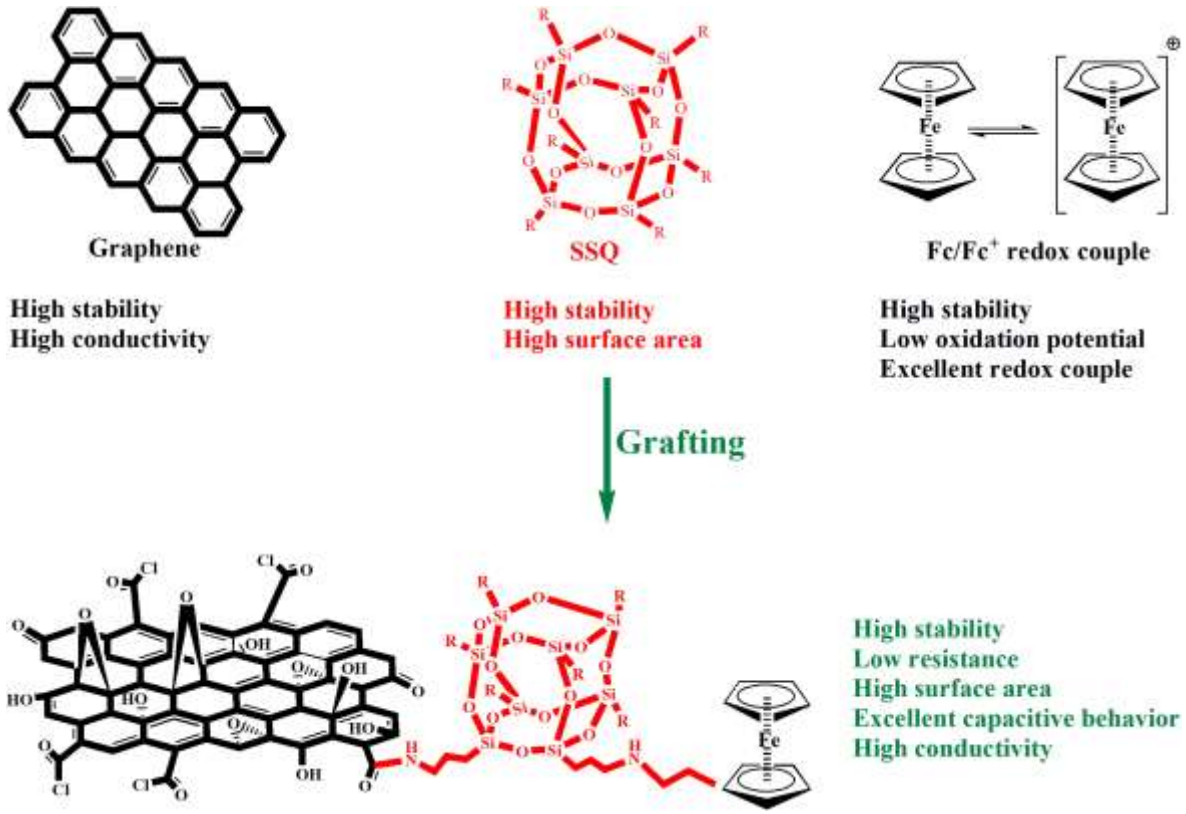

Fig. 17. A simple schematic of the GO-Amine-SSQ-Fc composite design and the results of this design

GO-Amine-SSQ-Fc composite is examined in the following subsection as positive and negative electrodes in a symmetric SC system.

3.2.2 Electrochemical performance of GO-Amine-SSQ-Fc//GO-Amine-SSQ-Fc system

To investigate the electrochemical behavior and energy storage mechanism of the GO-Amine-SSQ-Fc//GO-Amine-SSQ-Fc system, CV was performed in a potential window of 0 to 1.0 V at scan rates of 5 to 100 mV s^{-1} (**Fig. 18a**). The quasi-rectangular shape of the CV diagrams suggests the combination of both EDL and pseudocapacitive mechanisms. Also, CV patterns are remained during various scan rates, which confirms the low resistance of the system [145, 146]. Also, specific capacitance changes at different scan rates (5 to 200 mV s^{-1}) are drawn in a graph (**Fig. 18b**). The specific capacities of GO-Amine-SSQ-Fc//GO-Amine-SSQ-Fc system at different current densities are as follows: 288 F g^{-1} at 5 mV s^{-1}; 253 F g^{-1} at 10 mV s^{-1}; 227 F g^{-1} at 20 mV s^{-1}; 206 F g^{-1} at 30 mV s^{-1}; 191 F g^{-1} at 40 mV s^{-1}; 178 F g^{-1} at 50 mV s^{-1}; 154 F g^{-1} at 75 mV s^{-1}; 143 F g^{-1} at 100 mV s^{-1}; 124 F g^{-1} at 200 mV s^{-1}. The CV results confirm the high performance and excellent electrochemical behavior of SCs based on hybrid materials.

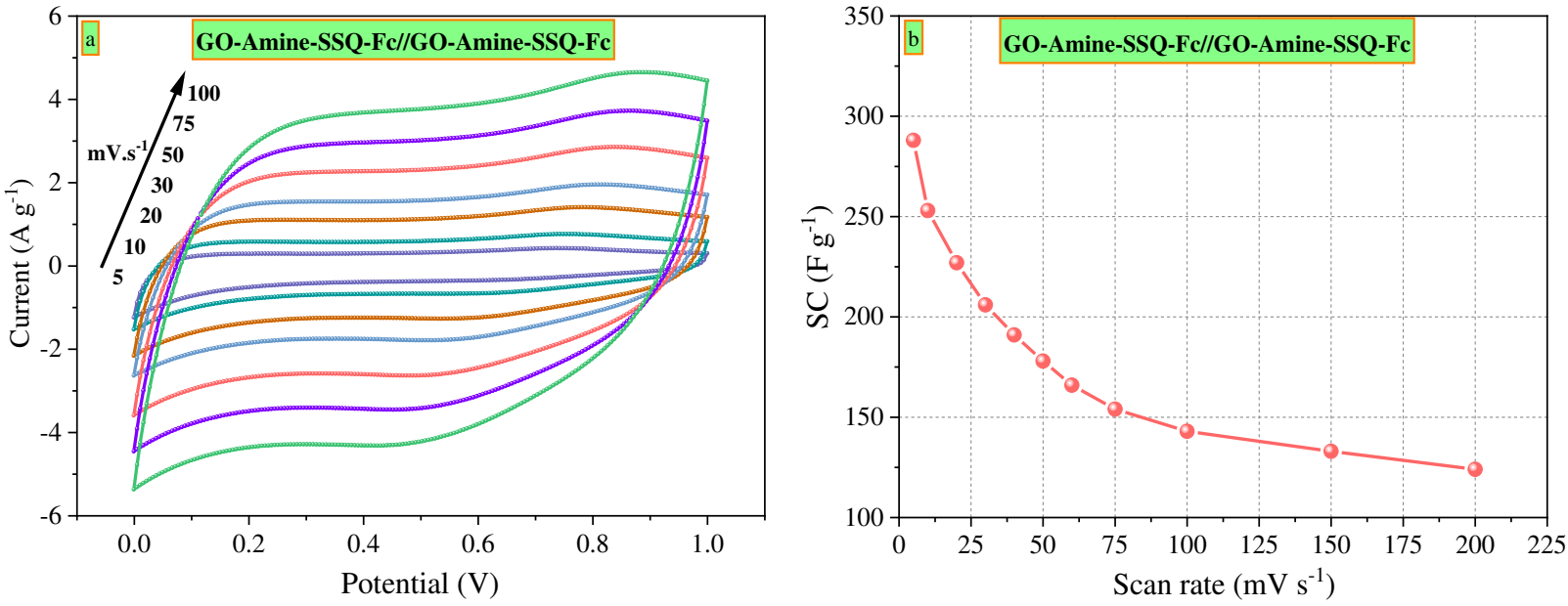

Fig. 18. a) CV diagrams of GO-Amine-SSQ-Fc//GO-Amine-SSQ-Fc system at scan rates of 5 to 100 mV s^{-1}, and **b)** Calculated specific capacities at various scan rates (5 to 200 mV s^{-1})

GCD test was utilized to evaluate the practical application of the GO-Amine-SSQ-Fc//GO-Amine-SSQ-Fc system. The GCD technique studies the shape of charge-discharge plots, stability during charge-discharge cycles, specific capacities, specific energy densities, and specific power densities. By GCD technique, the shape of charge-discharge plots, discharge times, stability during charge-discharge cycles, specific capacities, specific energy densities, and specific power densities were studied. The shape of the charge-discharge diagrams at different current densities are shown in **Fig. 19a**. The curves have a quasi-triangular shape originating from the EDL capacitive and pseudocapacitive behavior of the system [147]. The specific capacities at different current densities are shown in **Fig. 19b**, which is as follows: 304 F g^{-1} at 0.5 A g^{-1}; 292 F g^{-1} at 1 A g^{-1}; 272 F g^{-1} at 2 A g^{-1}; 224 F g^{-1} at 4 A g^{-1}; 160 F g^{-1} at 8 A g^{-1}; 96 F g^{-1} at 16 A g^{-1}. Values prove the excellent capacitance of the system. Ragone plots (specific energy (Wh Kg^{-1}) vs. specific power (W Kg^{-1})) are used to compare the performance of different energy storage devices. The Ragone plot of the GO-Amine-SSQ-Fc//GO-Amine-SSQ-Fc system can be seen in **Fig. 19c**. The symmetric SC system has a specific energy of 10.14 Wh Kg^{-1} at a specific power of 500 W Kg^{-1}. The system shows high both specific power and specific energy. Since the high retention capacitance is an important parameter for evaluating the energy storage devices, charge-discharge cycles were analyzed for 10000 consecutive cycles at 16 A g^{-1} (**Fig. 19d**). The system achieved retention capacitance of 92.5% over 10000 charge-discharge cycles, which guarantees high stability for long-term usage.

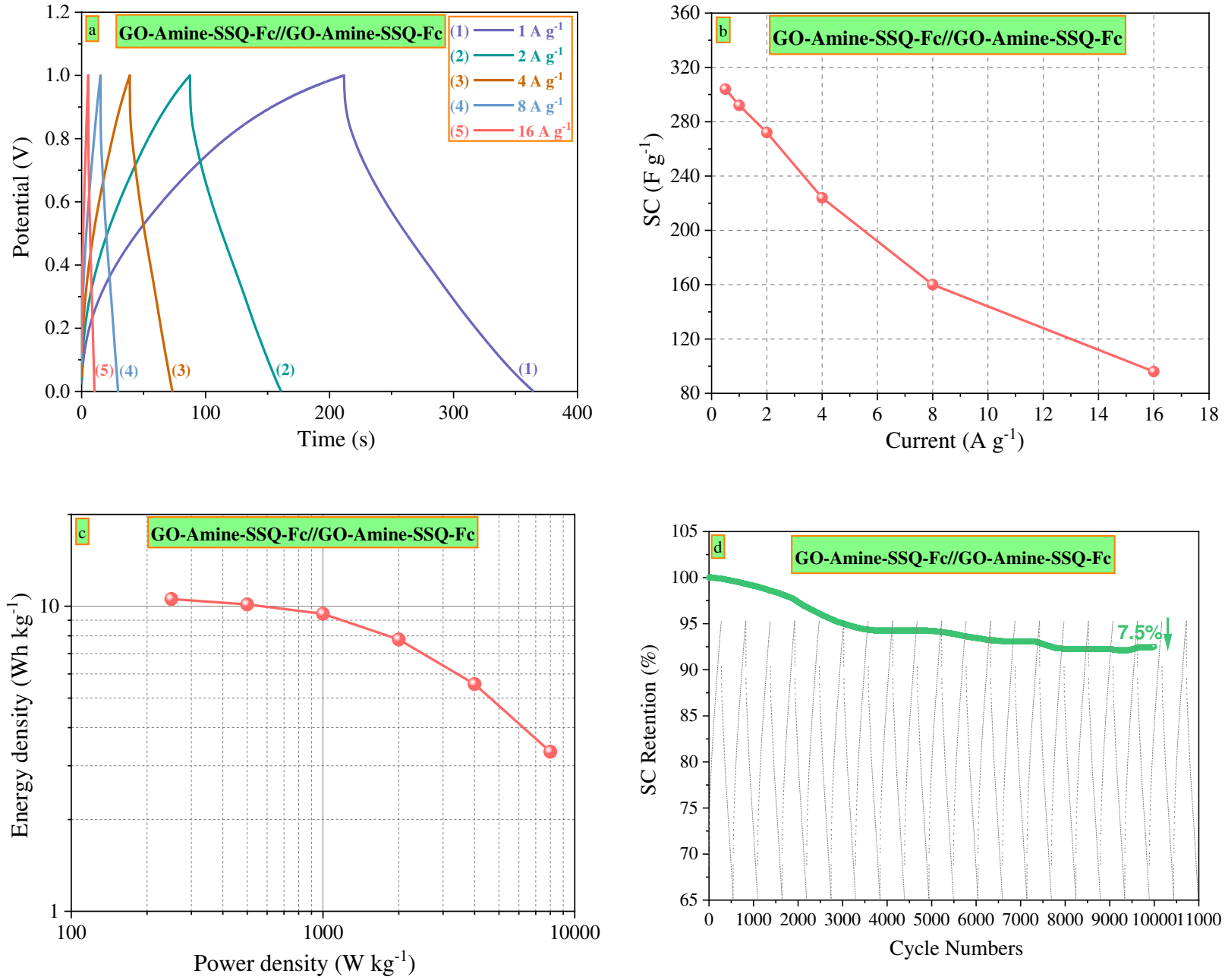

Fig. 19. a) GCD diagrams at current densities of 1 to 16 A g^{-1}, **b)** Calculated specific capacities at various current densities (0.5 to 16 A g^{-1}), **c)** Ragone plot, and **d)** Retention capacities during 5000 charge-discharge cycles

Low resistance, ideal specific capacity, high specific power, high specific energy, and excellent retention capacity confirm the system's applicability.

4. Computational methodology

In the present study, the theoretical charge density distribution analysis of the GO-Amine-SSQ-Fc composite on the basis of Bader's Atoms in Molecules (AIM) [148] analysis was performed. Prior to topological analysis, the GO-Amine-SSQ-Fc complex was optimized using density functional theory (DFT) [149, 150]. The hybrid DFT calculations were carried out employing Becke Lee-Yang-Parr (B3LYP) [151] hybrid functional in Vienna Ab Initio Simulation Package VASP [152]. The electron-ionic core interactions were described using the Projector augmented wave (PAW) potentials [153], considering dispersion correction of Grimme to include the Van der Waals interactions [154], where the cutoff energy of a plane-wave basis set was set to 500 eV. The Monkhorst-Pack [155] scheme of Brillouin zone sampling was applied with the k-point grid of 1×1×1. The geometry optimization was stopped when the force on each ion was less than 0.01 eV/Å and total energy converged to within 10^{-5} eV.

Then, the charge density information obtained was used from VASP optimization as inputs to the AIM-UC [156] package to calculate the topological properties and electron density distribution of GO-Amine-SSQ-Fc complex at the bond critical points (BCP) of C−C bonds of the GO layer. The critical point search has been done for the (3,-1) type critical points of C−C bonds of the structures [157]. The calculations were done using Quantum Theory of Atoms in Molecules (QTAIM), [157-159] where analysis of the Laplacian of electron density distribution over the atomic basins help us to identify the amount of atomic charges (electrons) and value of the concentration or depletion of charge density. the same calculations for the pristine GO layer were performed to see the effect of the functionalization on the charge density distribution on the GO layer.

First, computing started from the graphene primitive cell to create a single layer of graphene. Beginning, a unit cell with the graphene monolayer was constructed at the middle where it is replicated into an infinite layer by the periodic boundary condition. Then, the GO monolayer by adding different O-containing functional groups of hydroxyl, carbonyl, and carboxyl randomly around the edge and on the basal plane of graphene sheet was constructed, based on the Lerf-Klinowski [160] model. Finally, the GO-Amine-SSQ-Fc complex by adding SSQ and Fc groups to GO layer was created. The optimized structure of GO-Amine-SSQ-Fc used in the calculations is shown in **Fig. 20**.

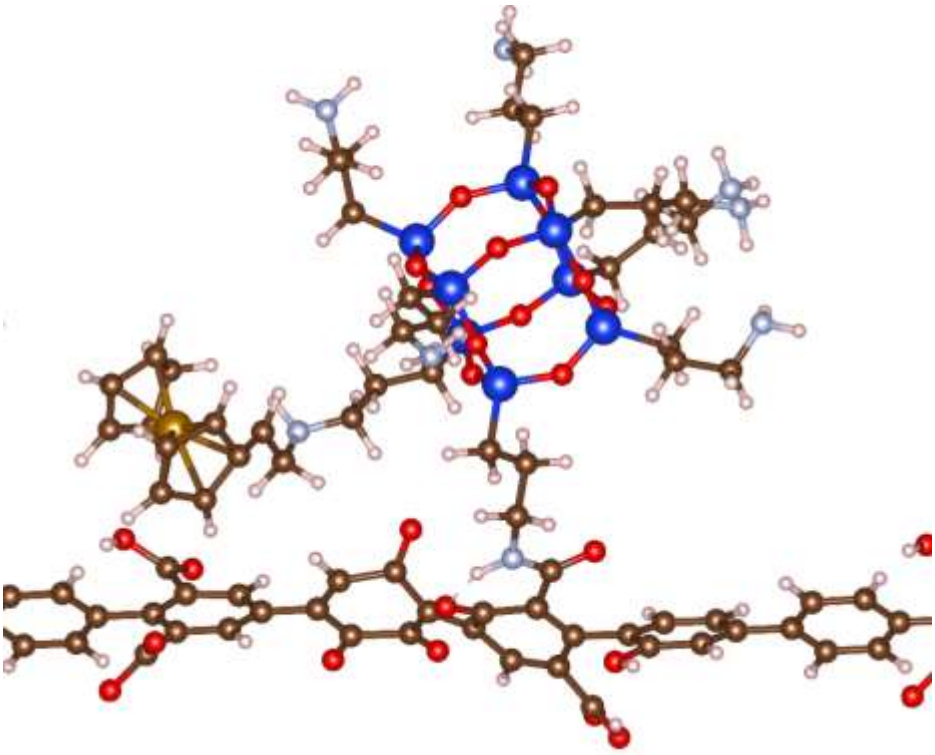

Fig. 20. The optimized structure of GO-Amine-SSQ-Fc (C, O, Si, N, Fe, and H atoms are shown in brown, red, dark blue, light blue, gold, and white spheres, respectively)

4.1 Computational results

To gain more insight into the charge density distribution of GO-Amine-SSQ-Fc electrode in supercapacitor devices, topological analysis of electron density $\rho_{bcp}(r)$ and its Laplacian $\nabla^2\rho_{bcp}(r)$ at their BCP was carried out, where the same analysis was done for the pristine GO layer. The values and differences of $\rho_{bcp}(r)$ and $\nabla^2{}_{\rho bc}\rho(r)$ of C−C bonds of pristine GO layer and GO-Amine-SSQ-Fc composite are represented in **Table 4** and **Fig. 22**, where all the corresponding carbon atoms of GO layer in the considered systems are presented in **Fig. 21**.

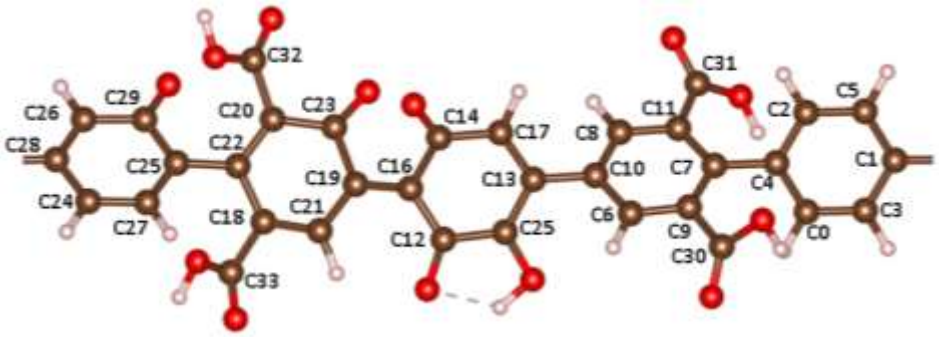

Fig. 21. The GO layer used in the DFT calculation (C, O, and H atoms are shown in brown, red, and white spheres, respectively)

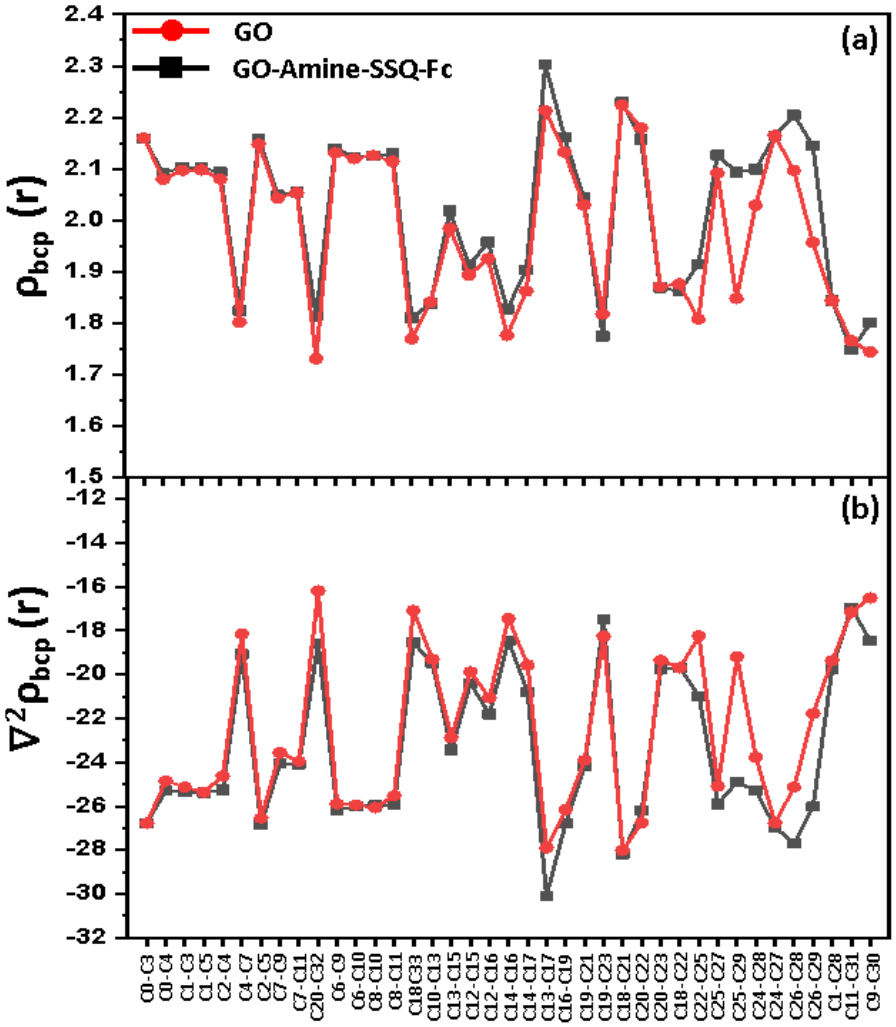

Fig. 22. The differences of the **a)** electron density ρ_{bcp}(r), and (b) Laplacian of electron density $\nabla^2\rho_{bcp}$(r) of C−C bonds at their bonding critical points (bcp) of pristine GO surface and GO layer of GO-Amine-SSQ-Fc complex (C, O, and H atoms are shown in brown, red, and white spheres, respectively)

Bonds	$\nabla^2\rho_{bcp}(r)$, $\rho_{bcp}(r)$ GO-Amine-SSQ-Fc	$\nabla^2\rho_{bcp}(r)$, $\rho_{bcp}(r)$ GO	Bonds	$\nabla^2\rho_{bcp}(r)$, $\rho_{bcp}(r)$ GO-Amine-SSQ-Fc	$\nabla^2\rho_{bcp}(r)$, $\rho_{bcp}(r)$ GO
C0-C3	-26.775, 2.159	-26.778, 2.160	**C18-C21**	-28.179, 2.230	-28.009, 2.224
C0-C4	-25.299, 2.092	-24.845, 2.080	**C20-C22**	-26.187, 2.157	-26.748, 2.179
C1-C3	-25.361, 2.091	-25.123, 2.097	**C20-C23**	-19.760, 1.869	-19.346, 1.871
C1-C5	-25.372, 2.103	-25.365, 2.098	**C18-C22**	-19.684, 1.862	-19.688, 1.876
C2-C4	-25.263, 2.093	-24.624, 2.080	**C22-C25**	-20.985, 1.914	-18.240, 1.808
C4-C7	-19.077, 1.824	-18.147, 1.802	**C25-C27**	-25.895, 2.126	-25.083, 2.092
C2-C5	-26.844, 2.158	-26.540, 2.148	**C25-C29**	-24.888, 2.093	-19.186, 1.848
C7-C9	-24.054, 2.048	-23.562, 2.043	**C24-C28**	-25.299, 2.099	-23.768, 2.029
C7-C11	-24.076, 2.054	-23.949, 2.054	**C24-C27**	-26.959, 2.165	-26.760, 2.165
C20-C32	-18.590, 1.814	-16.189, 1.731	**C26-C28**	-27.682, 2.204	-25.124, 2.097
C6-C9	-26.190, 2.139	-25.894, 2.131	**C26-C29**	-26.015, 2.145	-21.779, 1.957
C6-C10	-25.992, 2.122	-25.943, 2.120	**C1-C28**	-19.725,1.844	-19.361, 1.844
C8-C10	-25.975, 2.125	-26.058, 2.126	**C11-C31**	-16.953, 1.748	-17.158, 1.766
C8-C11	-25.954, 2.129	-25.516, 2.115	**C9-C30**	-18.460, 1.800	-16.510, 1.744
C18-C33	-18.542, 1.811	-17.081, 1.769			
C10-C13	-19.463, 1.838	-19.294, 1.841			
C13-C15	-23.431, 2.018	-22.869, 1.984			
C12-C15	-20.392, 1.912	-19.872, 1.893			
C12-C16	-21.809, 1.958	-20.052, 1.925			
C14-C16	-17.450, 1.828	-18.469, 1.776			
C14-C17	-20.792, 1.903	-19.568, 1.862			
C13-C17	-30.079, 2.303	-27.902, 2.213			
C16-C19	-26.871, 2.162	-26.150, 2.132			
C19-C21	-24.175, 2.043	-23.898, 2.030			
C19-C23	-17.470, 1.774	-18.249, 1.818			

Table 4. The topological properties of electron density of carbon bonds on GO layer of GO-Amine-SSQ-Fc complex. The values for a pristine GO surface are also provided. For finding the atoms refer to the **Fig. 20**.

Also, $\nabla^2_{\rho bc}\rho(r)$ of GO layer of GO-Amine-SSQ-Fc is plotted in **Fig.23** indicating accumulation of charge density between the bonds, where the positive (red contours) and negative (blue contours) imply charge concentration and depletion, respectively. The ranges of electron density of C−C bonds of pristine GO layer are 1.731 to 2.224 eÅ^{-3} with average of 1.988 eÅ^{-3} compared to those of 1.748 to 2.303 eÅ^{-3} and average of 2.020 eÅ^{-3} on GO layer of the GO-Amine-SSQ-Fc complex, respectively. For Laplacian of C−C bonds at their bonding critical points, in case of pristine GO layer, the results revealed ranges of -16.189 to -28.009 eÅ^{-5} with average of -22.531 eÅ^{-5}, while

ranges of -16.953 to -30.079 eÅ^{-5} with average of -23.381 eÅ^{-5} were obtained for GO layer of GO-Amine-SSQ-Fc complex. The results indicate that the electron densities distributions of most C–C bonds of GO layer are increased and the bond charges are more concentrated on GO-Amine-SSQ-Fc compared to those on pristine GO surface, which are due to the interactions of the connected SSQ and Fc to the GO layer in the GO-Amine-SSQ-Fc complex, which makes it more effective as an electrode material for SC.

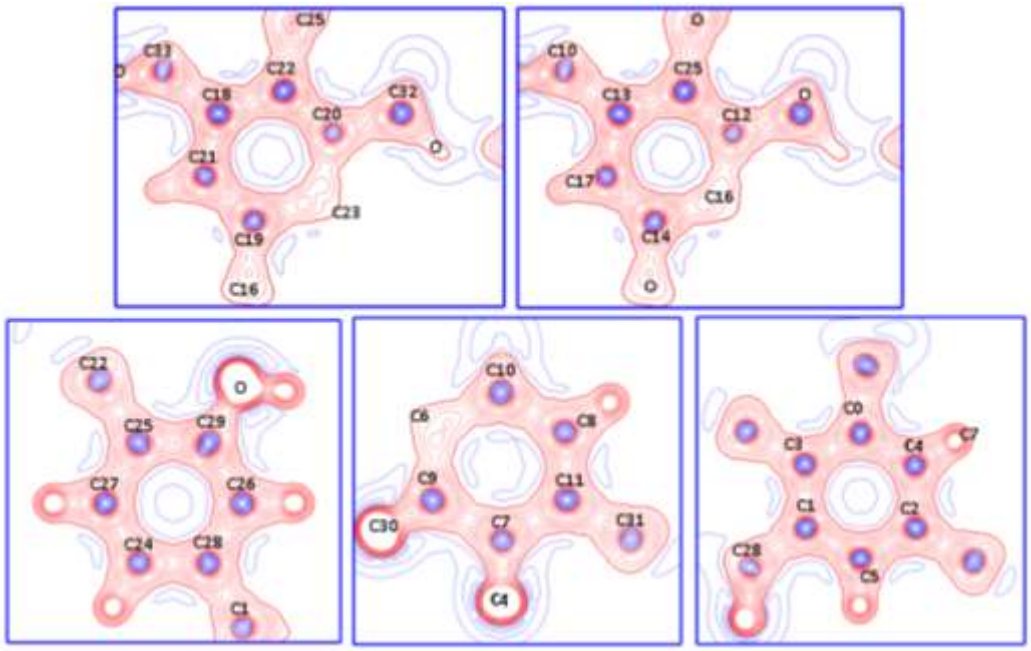

Fig. 23. The contour line plots of Laplacian of electron density of five phenyl rings of GO layer of GO-Amine-SSQ-Fc obtained from charge density calculation. Contours are drawn in 5 eÅ^{-5} intervals. The red and blue lines represent positive and negative values of Laplacian, respectively (C, O, and H atoms are shown in brown, red, and white spheres, respectively)

5. Conclusion

Herein, structural and electrochemical properties of GO-Amine-SSQ-Fc composite were characterized after chemical synthesis. The composite showed a specific surface area of 130.85 m^2 g^{-1}, which can be due to the presence of SSQ groups in the composite structure. Both energy storage mechanisms (faradaic and non-faradaic mechanisms) were confirmed by electrochemical tests. GO-Amine-SSQ-Fc composite in 3E system recorded specific capacitance of 574 F g^{-1} at 1 A g^{-1}, and retention capacitance of 90.1% over 10000 cycles. The prepared composite was also compared with other electrodes containing similar components, and its superiority was confirmed. Then, a symmetric supercapacitor device was assembled with positive and negative electrodes containing GO-Amine-SSQ-Fc composite that guaranteed excellent capacitive behavior. In

addition to the high specific capacity (304 F g^{-1} at 0.5 A g^{-1}), the device showed good retention capacity (92.5% after 10000 cycles). Also, system recorded specific energy of 10.14 Wh Kg^{-1} at a specific power of 500 W Kg^{-1}. The results exhibit the high potential of the GO-Amine-SSQ-Fc//GO-Amine-SSQ-Fc system in practical application. The computational results indicate that the electron densities distributions of most C–C bonds of GO layer are increased and the bond charges are more concentrated on GO-Amine-SSQ-Fc compared to those on pristine GO surface, which are due to the interactions of the connected SSQ and Fc to the GO layer in the GO-Amine-SSQ-Fc composite, which makes it more effective as an electrode material for supercapacitor.

Acknowledgment

The authors would like to gratefully thank Amirkabir University of Technology (AUT), Tehran, Iran, for their financial support. Author Seeram Ramakrishna acknowledges the IAF-PP project-R-265-000-A50-281 "Sustainable Tropical Data Centre Test Bed" awarded by the National Research Foundation of Singapore. The calculations presented in this study were also performed using the computing facilities of the Advanced Research Computing @ Cardiff (ARCCA) division, Cardiff University, UK.

References

1. Sekar, K., et al., *Ultrathin VS2 nanosheets vertically aligned on NiCo2S4@C3N4 hybrid for asymmetric supercapacitor and alkaline hydrogen evolution reaction.* Applied Surface Science, 2020. **527**: p. 146856.
2. Olabi, A.G., et al., *Critical review of energy storage systems.* Energy, 2021. **214**: p. 118987.
3. Aliakbari, R., et al., *Comprehensive study on poly ortho-aminophenol composite electrodes and their utilization for supercapacitor applications and green energy storage: A review.* Journal of Energy Storage, 2021. **44**: p. 103365.
4. Tobi, A.R. and J.O. Dennis, *Activated carbon from composite of palm bio-waste as electrode material for solid-state electric double layer capacitor.* Journal of Energy Storage, 2021. **42**: p. 103087.
5. Wei, Y., et al., *All pseudocapacitive MXene-MnO2 flexible asymmetric supercapacitor.* Journal of Energy Storage, 2022. **45**: p. 103715.
6. Tahir, M.A., N. Arshad, and M. Akram, *Recent advances in metal organic framework (MOF) as electrode material for super capacitor: A mini review.* Journal of Energy Storage, 2021: p. 103530.
7. Lu, L., et al., *Preparation of metal sulfide electrode materials derived based on metal organic framework and application of supercapacitors.* Journal of Energy Storage, 2022. **49**: p. 104073.
8. Zhao, Y., et al., *Intercalation pseudocapacitance in ZnS@C sheets composites for enhanced electrochemical energy storage.* Journal of Energy Storage, 2021. **39**: p. 102611.
9. Wang, P., et al., *A dual-polymer strategy boosts hydrated vanadium oxide for ammonium-ion storage.* Journal of Colloid and Interface Science, 2022. **606**: p. 1322-1332.
10. Wang, S., et al., *Synthesis of nickel-metal organic framework nanoplates with pyridine modulation and application to supercapacitors.* Journal of Energy Storage, 2021. **38**: p. 102528.

11. Balamurugan, J., et al., *Flexible Solid-State Asymmetric Supercapacitors Based on Nitrogen-Doped Graphene Encapsulated Ternary Metal-Nitrides with Ultralong Cycle Life.* Advanced Functional Materials, 2018. **28**(44): p. 1804663.
12. Muralee Gopi, C.V.V., R. Ramesh, and H.-J. Kim, *Designing nanosheet manganese cobaltate@manganese cobaltate nanosheet arrays as a battery-type electrode material towards high-performance supercapacitors.* Journal of Energy Storage, 2021: p. 103603.
13. Yuan, C., et al., *Preparation of cellulose-based carbon nanofibers/NiCo2S4 composites for high-performance all-solid-state symmetric supercapacitors.* Journal of Energy Storage, 2021: p. 103589.
14. Marfavi, Y., et al., *Application of ionic liquids in green energy-storage materials*, in *Ionic Liquid-Based Technologies for Environmental Sustainability*. 2022, Elsevier. p. 155-166.
15. Poochai, C., et al., *Waste coffee grounds derived nanoporous carbon incorporated with carbon nanotubes composites for electrochemical double-layer capacitors in organic electrolyte.* Journal of Energy Storage, 2021. **43**: p. 103169.
16. Bashir, S., et al., *Self-healable poly (N, N-dimethylacrylamide)/poly (3,4-ethylenedioxythiophene) polystyrene sulfonate composite hydrogel electrolytes for aqueous supercapacitors.* Journal of Energy Storage, 2022. **45**: p. 103760.
17. Chen, X.Y., et al., *Porosity-Engineered Carbon Materials for Supercapacitors: The Template Effect and the Improved Capacitive Performances by the Addition of Redox Additive.* Nano, 2018. **13**(08): p. 1850096.
18. Li, C., et al., *Polyvinyl alcohol/quaternary ammonium chitosan hydrogel electrolyte for sensing supercapacitors with excellent performance.* Journal of Energy Storage, 2022. **46**: p. 103918.
19. Du, P., et al., *Graphene-Wrapped Polyaniline Nanowire Array Modified Functionalized of Carbon Cloth for High-Performance Flexible Solid-State Supercapacitor.* ACS Sustainable Chemistry & Engineering, 2018. **6**(11): p. 14723-14733.
20. Du, P., et al., *Fabrication of uniform MnO2 layer-modified activated carbon cloth for high-performance flexible quasi-solid-state asymmetric supercapacitor.* Journal of Materials Science, 2022: p. 1-16.
21. Xu, L.H., et al., *Deep eutectic solvents as effective electrolyte from potassium iodide and ethylene glycol exhibiting redox behavior for supercapacitor application.* Journal of Energy Storage, 2022. **48**: p. 103955.
22. Zhong, M., et al., *A novel electrolyte of ternary deep eutectic solvent for wide temperature region supercapacitor with superior performance.* Journal of Energy Storage, 2020. **32**: p. 101904.
23. Samdhyan, K., et al., *Development of carbon-based copper sulfide nanocomposites for high energy supercapacitor applications: A comprehensive review.* Journal of Energy Storage, 2022. **46**: p. 103886.
24. Aparna, M.L., G.R. Rao, and T. Thomas, *Momordica Charantia pericarp derived activated carbon with dual redox additive electrolyte for high energy density supercapacitor devices.* Journal of Energy Storage, 2022. **48**: p. 104048.
25. Tafete, G.A., M.K. Abera, and G. Thothadri, *Review on nanocellulose-based materials for supercapacitors applications.* Journal of Energy Storage, 2022. **48**: p. 103938.
26. Zhu, P., et al., *Hollow cobalt-iron prussian blue analogue nanocubes for high-performance supercapacitors.* Journal of Energy Storage, 2020. **31**: p. 101544.
27. Veerapandi, G., et al., *Pseudo spin-ladder CaCu2O3 nanostructures as potential electrode material for asymmetric supercapacitors.* Journal of Energy Storage, 2022. **48**: p. 104051.
28. Heydari, H., et al., *Facile electrosynthesis and characterization of Poly Ortho Amino Phenol/MoS2/MnO2 nanocomposite as a new supercapacitor.* Journal of Energy Storage, 2022. **48**: p. 103905.

29. Zhang, F., et al., *Fabrication of defect-rich bifunctional hollow NiTe2 nanotubes for high performance hydrogen evolution electrocatalysts and supercapacitors.* Journal of Energy Storage, 2021. **42**: p. 103098.
30. Balamurugan, J., et al., *Hierarchical design of Cu1−xNixS nanosheets for high-performance asymmetric solid-state supercapacitors.* Journal of Materials Chemistry A, 2017. **5**(37): p. 19760-19772.
31. Zhang, Y., et al., *Bamboo Leaves as Sustainable Sources for the Preparation of Amorphous Carbon/Iron Silicate Anode and Nickel–Cobalt Silicate Cathode Materials for Hybrid Supercapacitors.* ACS Applied Energy Materials, 2021. **4**(9): p. 9328-9340.
32. Jing, X., et al., *Layered silicate magadiite–derived three-dimensional honeycomb-like cobalt–nickel silicates as excellent cathode for hybrid supercapacitors.* Materials Today Chemistry, 2021. **22**: p. 100550.
33. Sardana, S., et al., *Conducting polymer hydrogel based electrode materials for supercapacitor applications.* Journal of Energy Storage, 2022. **45**: p. 103510.
34. Liu, B., et al., *Facile fabrication of oxygen and nitrogen co-doped 3D-carbon nanoarrays for high performance environmentally friendly wireless charging integration supercapacitor.* Journal of Energy Storage, 2022. **49**: p. 104082.
35. Nath, A.R., et al., *Enhancing the stability of electrochemical asymmetric supercapacitor by incorporating thiophene-pyrrole copolymer with nickel sulfide/nickel hydroxide composite.* Journal of Energy Storage, 2022. **46**: p. 103833.
36. Jiang, G., et al., *Hierarchically porous carbon derived from magnesium-based metal-organic frameworks as advanced active material for supercapacitor.* Journal of Energy Storage, 2022. **49**: p. 104071.
37. Yang, W., et al., *Manganese-doped cobalt zeolitic imidazolate framework with highly enhanced performance for supercapacitor.* Journal of Energy Storage, 2019. **26**: p. 101018.
38. Du, P., et al., *Fabrication of hierarchical porous nickel based metal-organic framework (Ni-MOF) constructed with nanosheets as novel pseudo-capacitive material for asymmetric supercapacitor.* Journal of Colloid and Interface Science, 2018. **518**: p. 57-68.
39. Oglou, R.C., et al., *Highly stable Megalopolis lignite based N and S self-doped hierarchically porous activated carbons for high performance supercapacitors and ash content effects on performance.* Journal of Energy Storage, 2022. **46**: p. 103817.
40. Ma, Q., et al., *Self-templating synthesis of hierarchical porous carbon with multi-heteroatom co-doping from tea waste for high-performance supercapacitor.* Journal of Energy Storage, 2022. **45**: p. 103509.
41. Liu, H., et al., *Tuning Nitrogen Species in Two-Dimensional Carbon through Pore Structure Change for High Supercapacitor Performance.* ChemElectroChem, 2019. **6**(20): p. 5220-5228.
42. Liu, H., et al., *Urea-Modified Phenol-Formaldehyde Resins for the Template-Assisted Synthesis of Nitrogen-Doped Carbon Nanosheets as Electrode Material for Supercapacitors.* ChemElectroChem, 2019. **6**(3): p. 885-891.
43. Balamurugan, J., et al., *Facile synthesis of vanadium nitride/nitrogen-doped graphene composite as stable high performance anode materials for supercapacitors.* Journal of Power Sources, 2016. **308**: p. 149-157.
44. Dong, X., et al., *Rational design of double-sandwich-like C@Co,CoO/Co2SiO4/rGO architectures boost electrochemical performances of Co2SiO4 for energy storage devices.* Chemical Engineering Journal, 2022. **431**: p. 133277.
45. Nithya, V.D., *A review on holey graphene electrode for supercapacitor.* Journal of Energy Storage, 2021. **44**: p. 103380.

46. Zhang, R. and H. Pang, *Application of graphene-metal/conductive polymer based composites in supercapacitors ☆.* Journal of Energy Storage, 2021. **33**: p. 102037.
47. Rao, S.S., *Synthesis of CNTs on ZnO/NiS composite as an advanced electrode material for high-performance supercapacitors.* Journal of Energy Storage, 2020. **28**: p. 101199.
48. Liu, D., et al., *Skeleton/skin structured (RGO/CNTs)@ PANI composite fiber electrodes with excellent mechanical and electrochemical performance for all-solid-state symmetric supercapacitors.* Journal of colloid and interface science, 2018. **513**: p. 295-303.
49. Balamurugan, J., et al., *Facile synthesis of 3D hierarchical N-doped graphene nanosheet/cobalt encapsulated carbon nanotubes for high energy density asymmetric supercapacitors.* Journal of Materials Chemistry A, 2016. **4**(24): p. 9555-9565.
50. Gopalsamy, K., et al., *Fabrication of nitrogen and sulfur co-doped graphene nanoribbons with porous architecture for high-performance supercapacitors.* Chemical Engineering Journal, 2017. **312**: p. 180-190.
51. Zhang, Z.J., et al., *Dual surface modification of carbon materials by polydopamine and phosphomolybdic acid for supercapacitor application.* Dalton Transactions, 2019. **48**(46): p. 17321-17330.
52. Selvam, S. and J.-H. Yim, *Multifunctional supercapacitor integrated sensor from Oyster and Cicada derived bio-ternary composite: Vanillin/caffeine detections in beverages.* Journal of Energy Storage, 2022. **45**: p. 103791.
53. Venkateshalu, S., et al., *Phosphorene, antimonene, silicene and siloxene based novel 2D electrode materials for supercapacitors-A brief review.* Journal of Energy Storage, 2022. **48**: p. 104027.
54. Deyab, M.A., et al., *Progress study on nickel ferrite alloy-graphene nanosheets nanocomposites as supercapacitor electrodes.* Journal of Energy Storage, 2022. **46**: p. 103926.
55. Vandana, M., et al., *Graphene oxide decorated SnO2 quantum dots/polypyrrole ternary composites towards symmetric supercapacitor application.* Journal of Energy Storage, 2022. **46**: p. 103904.
56. Du, P., H. Kang, and Y. Dong, *Carbon dots regulate crosslinking of functionalized three-dimensional graphene networks decorated with p-phenylenediamine for superior performance flexible solid-state supercapacitors.* Journal of Energy Storage, 2020. **30**: p. 101586.
57. Mohanadas, D., N.H.N. Azman, and Y. Sulaiman, *A bifunctional asymmetric electrochromic supercapacitor with multicolor property based on nickel oxide/vanadium oxide/reduced graphene oxide.* Journal of Energy Storage, 2022. **48**: p. 103954.
58. Liu, J., et al., *Mild synthesis of holey N-doped reduced graphene oxide and its double-edged effects in polyaniline hybrids for supercapacitor application.* Electrochimica Acta, 2019. **305**: p. 175-186.
59. Sekar, K., et al., *Boosting the electrochemical performance of MoS2 nanospheres-N-doped-GQDs-rGO three-dimensional nanostructure for energy storage and conversion applications.* Applied Surface Science, 2020. **504**: p. 144441.
60. Dong, X., et al., *Sandwich-like honeycomb Co2SiO4/rGO/honeycomb Co2SiO4 structures with enhanced electrochemical properties for high-performance hybrid supercapacitor.* Journal of Power Sources, 2021. **492**: p. 229643.
61. Sreejith, S., X. Ma, and Y. Zhao, *Graphene oxide wrapping on squaraine-loaded mesoporous silica nanoparticles for bioimaging.* Journal of the American Chemical Society, 2012. **134**(42): p. 17346-17349.
62. Lakra, R., et al., *A mini-review: Graphene based composites for supercapacitor application.* Inorganic Chemistry Communications, 2021. **133**: p. 108929.
63. Ro, H.W. and C.L. Soles, *Silsesquioxanes in nanoscale patterning applications.* Materials Today, 2011. **14**(1-2): p. 20-33.

64. Dong, F., L. Lu, and C.S. Ha, *Silsesquioxane-Containing Hybrid Nanomaterials: Fascinating Platforms for Advanced Applications.* Macromolecular Chemistry and Physics, 2019. **220**(3): p. 1800324.
65. Kaniewska, K., J. Romański, and M. Karbarz, *Oxidation of ferrocenemethanol grafted to a hydrogel network through cysteine for triggering volume phase transition.* RSC Advances, 2013. **3**(45): p. 23816-23823.
66. Rabti, A., N. Raouafi, and A. Merkoçi, *Bio (sensing) devices based on ferrocene–functionalized graphene and carbon nanotubes.* Carbon, 2016. **108**: p. 481-514.
67. Hummers, W.S. and R.E. Offeman, *Preparation of Graphitic Oxide.* Journal of the American Chemical Society, 1958. **80**(6): p. 1339-1339.
68. Männle, F., et al., *Polymer nanocomposite coatings based on polyhedral oligosilsesquioxanes: route for industrial manufacturing and barrier properties.* Journal of Nanoparticle Research, 2011. **13**(10): p. 4691-4701.
69. Yang, X. and H. Liu, *Ferrocene-Functionalized Silsesquioxane-Based Porous Polymer for Efficient Removal of Dyes and Heavy Metal Ions.* Chemistry–A European Journal, 2018. **24**(51): p. 13504-13511.
70. Telegdi, J., A. Shaban, and G. Vastag, *Biocorrosion—Steel*, in *Encyclopedia of Interfacial Chemistry*, K. Wandelt, Editor. 2018, Elsevier: Oxford. p. 28-42.
71. Costa, R., et al., *Assigning XPS features in B, N-doped graphene: input from ab initio quantum chemical calculations.* Physical Chemistry Chemical Physics, 2021. **23**(2): p. 1558-1565.
72. Zheng, P., et al., *N-doped graphene-wrapped TiO2 nanotubes with stable surface Ti3+ for visible-light photocatalysis.* Applied Surface Science, 2020. **512**: p. 144549.
73. Woldetinsay, M., et al., *Synergetic effect between MoS2 and N, S- doped reduced graphene oxide supported palladium nanoparticles for hydrogen evolution reaction.* Materials Chemistry and Physics, 2020. **251**: p. 123106.
74. Li, B., et al., *Photochemical chlorination of graphene.* ACS nano, 2011. **5**(7): p. 5957-5961.
75. Ajdari, F.B., et al., *Electrochemical performance of Silsesquioxane-GO loaded with alkoxy substituted ammonium-based ionic liquid and POAP for supercapacitor.* Electrochimica Acta, 2020. **354**: p. 136663.
76. Ma, J., et al., *Preliminary study on pyrolysis of polymethylsilsesquioxane by FT-IR and XPS.* 2002.
77. Zhang, X., et al., *Corrosion resistance of organic coating based on polyhedral oligomeric silsesquioxane-functionalized graphene oxide.* Applied Surface Science, 2019. **484**: p. 814-824.
78. Christopher, G., M. Anbu Kulandainathan, and G. Harichandran, *Comparative study of effect of corrosion on mild steel with waterborne polyurethane dispersion containing graphene oxide versus carbon black nanocomposites.* Progress in Organic Coatings, 2015. **89**: p. 199-211.
79. Zong, P., et al., *Effect of aminopropylisobutyl polyhedral oligomeric silsesquioxane functionalized graphene on the thermal conductivity and electrical insulation properties of epoxy composites.* RSC advances, 2016. **6**(13): p. 10498-10506.
80. Xue, Y., et al., *Functionalization of Graphene Oxide with Polyhedral Oligomeric Silsesquioxane (POSS) for Multifunctional Applications.* The Journal of Physical Chemistry Letters, 2012. **3**(12): p. 1607-1612.
81. Vinod, K.R., et al., *Insights into the nitridation of zero-valent iron nanoparticles for the facile synthesis of iron nitride nanoparticles.* RSC advances, 2016. **6**(51): p. 45850-45857.
82. Han, D., et al., *Facile construction of porous magnetic nanoparticles from ferrocene-functionalized polyhedral oligomeric silsesquioxane-containing microparticles for dye adsorption.* Industrial & Engineering Chemistry Research, 2020. **59**(20): p. 9532-9540.
83. Kaneko, Y., et al., *Silsesquioxanes: Recent advancement and novel applications*. 2012, Hindawi.

84. Fontanesi, C., et al., *Redox-Active Ferrocene grafted on H-Terminated Si (111): Electrochemical Characterization of the Charge Transport Mechanism and Dynamics.* Scientific reports, 2019. **9**(1): p. 1-7.
85. Valentini, L., et al., *POSS vapor grafting on graphene oxide film.* Chemical Physics Letters, 2012. **537**: p. 84-87.
86. Valentini, L., et al., *Deposition of amino-functionalized polyhedral oligomeric silsesquioxanes on graphene oxide sheets immobilized onto an amino-silane modified silicon surface.* Journal of Materials Chemistry, 2012. **22**(13): p. 6213-6217.
87. Yang, X. and H. Liu, *Diphenylphosphine-substituted ferrocene/silsesquioxane-based hybrid porous polymers as highly efficient adsorbents for water treatment.* ACS applied materials & interfaces, 2019. **11**(29): p. 26474-26482.
88. Rahimpour, K. and R. Teimuri-Mofrad, *Star-Shaped Ferrocene-Based 1, 4-Disubstituted-1, 2, 3-Triazole Derivatives: Synthesis, Characterization, and Investigation of Linear Optical and Electrochemical Properties.* Applied Organometallic Chemistry, 2020. **34**(11): p. e5943.
89. Alhathir, A., *Synthesis and Electrochemical Study of Copolymers Containing Ferrocene and Imidazole.* 2017.
90. Li, C., et al., *Crosslinking-induced spontaneous growth: a novel strategy for synthesizing sandwich-type graphene@ Fe3O4 dots/amorphous carbon with high lithium storage performance.* Chemical Engineering Journal, 2018. **334**: p. 1614-1620.
91. Teimuri-Mofrad, R., K.D. Safa, and K. Rahimpour, *Synthesis, characterization and electrochemical properties of novel trinuclear ferrocenyl based organosilane compounds.* Journal of Organometallic Chemistry, 2014. **758**: p. 36-44.
92. Teimuri-Mofrad, R., K. Rahimpour, and A. Aghaiepour, *New ethylferrocenyl based pyranylidene bridge dyads: Synthesis, characterization and investigation of electrochemical and optical properties.* Journal of Organometallic Chemistry, 2019. **896**: p. 16-23.
93. Ma, Q., et al., *A ferrocene-containing porous organic polymer linked by tetrahedral silicon-centered units for gas sorption.* Applied Organometallic Chemistry, 2018. **32**(1): p. e3935.
94. Wang, X., et al., *Simultaneous reduction and surface functionalization of graphene oxide with POSS for reducing fire hazards in epoxy composites.* Journal of Materials Chemistry, 2012. **22**(41): p. 22037-22043.
95. Kowsari, E. and M.R. Chirani, *High efficiency dye-sensitized solar cells with tetra alkyl ammonium cation-based ionic liquid functionalized graphene oxide as a novel additive in nanocomposite electrolyte.* Carbon, 2017. **118**: p. 384-392.
96. Huang, Y., et al., *Extremely sensitive, allochroic airflow sensors by synergistic effect of reversible water molecules adsorption and tunable interlayer distance in graphene oxide film.* Advanced Materials Interfaces, 2019. **6**(9): p. 1900365.
97. Panahi-Sarmad, M., et al., *Tuning the surface chemistry of graphene oxide for enhanced dielectric and actuated performance of silicone rubber composites.* ACS Applied Electronic Materials, 2019. **1**(2): p. 198-209.
98. Tamaki, R., J. Choi, and R.M. Laine, *A polyimide nanocomposite from octa (aminophenyl) silsesquioxane.* Chemistry of materials, 2003. **15**(3): p. 793-797.
99. Wang, Y., F. Liu, and X. Xue, *Morphology and properties of UV-curing epoxy acrylate coatings modified with methacryl-POSS.* Progress in Organic Coatings, 2015. **78**: p. 404-410.
100. Preuß, A., et al., *Ferrocenyl naphthalenes: Substituent-and substitution pattern-depending charge transfer studies.* Dalton Transactions, 2019. **48**(38): p. 14418-14432.
101. Brock, C.P. and Y. Fu, *Rigid-body disorder models for the high-temperature phase of ferrocene.* Acta Crystallographica Section B: Structural Science, 1997. **53**(6): p. 928-938.

102. Shi, Y.-C., C.-X. Sui, and J.-J. Wu, *(S)-3-[(1-Ethoxy-carbonyl-2-phenyl-ethyl)amino]-1-ferrocenylbut-2-en-1-one.* Acta Crystallographica Section E, 2005. **61**(9): p. m1878-m1879.
103. Muñiz, K. and M. Nieger, *Ferrocenoyl-substituted Cinchona alkaloids: synthesis, structure, and application in asymmetric catalytic oxidation.* Organometallics, 2003. **22**(22): p. 4616-4619.
104. Tombul, M., et al., *1, 4-Diferrocenylbutane-1, 4-dione.* Acta Crystallographica Section E: Structure Reports Online, 2008. **64**(3): p. m444-m445.
105. Chai, J.-H. and Q.-S. Wu, *Electrospinning preparation and electrical and biological properties of ferrocene/poly (vinylpyrrolidone) composite nanofibers.* Beilstein journal of nanotechnology, 2013. **4**(1): p. 189-197.
106. Zhan, Y., et al., *Iodine/nitrogen co-doped graphene as metal free catalyst for oxygen reduction reaction.* Carbon, 2015. **95**: p. 930-939.
107. Ashtiani, A.A., et al., *Synthesis of novel functionalized graphene oxide with incorporation pyrimidine group including cobalt-iodine bonds their nanocomposites with p-type conductive polymer as excellent pseudocapacitor electrode materials.* Journal of Materials Science: Materials in Electronics, 2019. **30**(20): p. 18439-18451.
108. Eckmann, A., et al., *Probing the nature of defects in graphene by Raman spectroscopy.* Nano letters, 2012. **12**(8): p. 3925-3930.
109. Ajdari, F.B., et al., *Melamine-functionalized graphene oxide: Synthesis, characterization and considering as pseudocapacitor electrode material with intermixed POAP polymer.* Applied Surface Science, 2018. **459**: p. 874-883.
110. Anwar, A., et al., *Enhanced properties of cementitious composite tailored with graphene oxide nanomaterial-a review.* Developments in the Built Environment, 2020. **1**: p. 100002.
111. Khalfaoui, M., et al., *New theoretical expressions for the five adsorption type isotherms classified by BET based on statistical physics treatment.* Journal of Colloid and Interface Science, 2003. **263**(2): p. 350-356.
112. Raja, P. and A. Barron, *BET Surface Area Analysis of Nanoparticles.* Chemistry LibreTexts, 2019.
113. Kathalingam, A., et al., *Nanosheet-like ZnCo2O4@nitrogen doped graphene oxide/polyaniline composite for supercapacitor application: Effect of polyaniline incorporation.* Journal of Alloys and Compounds, 2020. **830**: p. 154734.
114. Askari, M.B. and P. Salarizadeh, *Binary nickel ferrite oxide (NiFe2O4) nanoparticles coated on reduced graphene oxide as stable and high-performance asymmetric supercapacitor electrode material.* International Journal of Hydrogen Energy, 2020. **45**(51): p. 27482-27491.
115. Schwanke, A.J., R. Balzer, and S. Pergher, *Chapter 49 - Mesoporous Materials for Reduction of Air Pollutants: Volatile Organic Compounds*, in *Handbook of Nanomaterials for Industrial Applications*, C. Mustansar Hussain, Editor. 2018, Elsevier. p. 908-915.
116. Stine, K.J., *Chapter Two - Application of Porous Materials to Carbohydrate Chemistry and Glycoscience*, in *Advances in Carbohydrate Chemistry and Biochemistry*, D.C. Baker, Editor. 2017, Academic Press. p. 61-136.
117. Barrett, E.P., L.G. Joyner, and P.P. Halenda, *The determination of pore volume and area distributions in porous substances. I. Computations from nitrogen isotherms.* Journal of the American Chemical society, 1951. **73**(1): p. 373-380.
118. Qin, Y., et al., *Anthraquinone-functionalized graphene framework for supercapacitors and lithium batteries.* Ceramics International, 2020. **46**(10): p. 15379-15384.
119. Masteri-Farahani, M. and M. Ghahremani, *Surface functionalization of graphene oxide and graphene oxide-magnetite nanocomposite with molybdenum-bidentate Schiff base complex.* Journal of Physics and Chemistry of Solids, 2019. **130**: p. 6-12.

120. Zhang, Y., et al., *Phenolic hydroxyl functionalized partially reduced graphene oxides for symmetric supercapacitors with significantly enhanced electrochemical performance.* Journal of Power Sources, 2019. **435**: p. 226799.
121. Vicente-Martínez, Y., et al., *Graphene oxide and graphene oxide functionalized with silver nanoparticles as adsorbents of phosphates in waters. A comparative study.* Science of The Total Environment, 2020. **709**: p. 136111.
122. Wang, Y., et al., *Supercapacitor devices based on graphene materials.* The Journal of Physical Chemistry C, 2009. **113**(30): p. 13103-13107.
123. Czepa, W., et al., *Reduced graphene oxide–silsesquioxane hybrid as a novel supercapacitor electrode.* Nanoscale, 2020. **12**(36): p. 18733-18741.
124. Teimuri-Mofrad, R., H. Abbasi, and R. Hadi, *Graphene oxide-grafted ferrocene moiety via ring opening polymerization (ROP) as a supercapacitor electrode material.* Polymer, 2019. **167**: p. 138-145.
125. Wang, Y., E.I. Rogers, and R.G. Compton, *The measurement of the diffusion coefficients of ferrocene and ferrocenium and their temperature dependence in acetonitrile using double potential step microdisk electrode chronoamperometry.* Journal of Electroanalytical Chemistry, 2010. **648**(1): p. 15-19.
126. Laoire, C.O., et al., *Electrochemical studies of ferrocene in a lithium ion conducting organic carbonate electrolyte.* Electrochimica Acta, 2009. **54**(26): p. 6560-6564.
127. Congiu, M., et al., *A novel and large area suitable water-based ink for the deposition of cobalt sulfide films for solar energy conversion with iodine-free electrolytes.* Solar Energy, 2015. **122**: p. 87-96.
128. Li, Z., Y. Zhang, and W. Zhang, *Controlled synthesis of CNTs/MoS2/Fe3O4 for high-performance supercapacitors.* Materials Research Express, 2017. **4**(5): p. 055018.
129. Kolathodi, M.S., et al., *Beaded manganese oxide (Mn 2 O 3) nanofibers: preparation and application for capacitive energy storage.* Journal of Materials Chemistry A, 2016. **4**(20): p. 7883-7891.
130. Xie, X., et al., *MoS2 nanosheets vertically aligned on carbon paper: a freestanding electrode for highly reversible sodium-ion batteries.* Advanced energy materials, 2016. **6**(5): p. 1502161.
131. Szubzda, B., A. Szmaja, and A. Halama, *Influence of structure and wettability of supercapacitor electrodes carbon materials on their electrochemical properties in water and organic solutions.* Electrochimica acta, 2012. **86**: p. 255-259.
132. Aziz, S.B., et al., *Development of polymer blend electrolyte membranes based on chitosan: Dextran with high ion transport properties for EDLC application.* International journal of molecular sciences, 2019. **20**(13): p. 3369.
133. Biesheuvel, P., S. Porada, and J. Dykstra, *The difference between Faradaic and non-Faradaic electrode processes.* arXiv preprint arXiv:1809.02930, 2018.
134. Hadi, R., et al., *Synthesis, Characterization and Electrochemical Properties of 4-Azidobutylferrocene-Grafted Reduced Graphene Oxide-Polyaniline Nanocomposite for Supercapacitor Applications.* ChemistrySelect, 2020. **5**(2): p. 575-583.
135. Zheng, X., et al., *Tunable ZnO/NiO heterojunction interface for supercapacitors electrodes by piezoelectric modulation.* Journal of Alloys and Compounds, 2021. **851**: p. 156902.
136. Madhu, R., et al., *Eco-friendly synthesis of activated carbon from dead mango leaves for the ultrahigh sensitive detection of toxic heavy metal ions and energy storage applications.* Rsc Advances, 2014. **4**(3): p. 1225-1233.
137. Adhikari, A.D., et al., *Polyaniline-Stabilized Intertwined Network-like Ferrocene/Graphene Nanoarchitecture for Supercapacitor Application.* Chemistry–An Asian Journal, 2017. **12**(8): p. 900-909.

138. Saha, S., et al., *A review on the heterostructure nanomaterials for supercapacitor application.* Journal of Energy Storage, 2018. **17**: p. 181-202.
139. Orazem, M.E. and B. Tribollet, *Electrochemical impedance spectroscopy*. New Jersey, 2008: p. 383-389.
140. Ali, G.A., et al., *Ferrocene functionalized multi-walled carbon nanotubes as supercapacitor electrodes.* Journal of Molecular Liquids, 2020. **318**: p. 114064.
141. Rahimpour, K. and R. Teimuri-Mofrad, *Novel hybrid supercapacitor based on ferrocenyl modified graphene quantum dot and polypyrrole nanocomposite.* Electrochimica Acta, 2020. **345**: p. 136207.
142. Zhang, X., et al., *Modular Preparation of Graphene-Based Functional Architectures through Two-Step Organic Reactions: Towards High-Performance Energy Storage.* Chemistry–A European Journal, 2018. **24**(69): p. 18518-18528.
143. AliAkbari, R., et al., *Recent studies on ionic liquids in metal recovery from E-waste and secondary sources by liquid-liquid extraction and electrodeposition: a review.* Materials Circular Economy, 2020. **2**(1): p. 1-27.
144. Bigdeloo, M., et al., *Review on innovative sustainable nanomaterials to enhance the performance of supercapacitors.* Journal of Energy Storage, 2021. **37**: p. 102474.
145. Ghadimi, L.S., et al., *Novel nanocomposite of MnFe2O4 and nitrogen-doped carbon from polyaniline carbonization as electrode material for symmetric ultra-stable supercapacitor.* Electrochimica Acta, 2018. **282**: p. 116-127.
146. Lu, H., et al., *Microcrystalline cellulose-derived porous carbons with defective sites for electrochemical applications.* Journal of Materials Chemistry A, 2019. **7**(39): p. 22579-22587.
147. Zhang, Z., et al., *Hierarchical porous nitrogen-doped graphite from tissue paper as efficient electrode material for symmetric supercapacitor.* Journal of Power Sources, 2021. **492**: p. 229670.
148. Bader, R., *Atoms in Molecules: A Quantum Theory: Oxford Univ.* Press.: Oxford, 1990.
149. Hohenberg, P. and W. Kohn, *Inhomogeneous Electron Gas.* Physical Review, 1964. **136**(3B): p. B864-B871.
150. Kohn, W. and L. Sham, *Physical Reviews 1965, 140.* A1133–A1138.
151. Becke, A.D., *A new mixing of Hartree–Fock and local density-functional theories.* The Journal of chemical physics, 1993. **98**(2): p. 1372-1377.
152. Kresse, G. and J. Furthmüller, *Efficiency of ab-initio total energy calculations for metals and semiconductors using a plane-wave basis set.* Computational materials science, 1996. **6**(1): p. 15-50.
153. Blöchl, P.E., *Projector augmented-wave method.* Physical Review B, 1994. **50**(24): p. 17953-17979.
154. Grimme, S., S. Ehrlich, and L. Goerigk, *Effect of the damping function in dispersion corrected density functional theory.* Journal of computational chemistry, 2011. **32**(7): p. 1456-1465.
155. Monkhorst, H.J. and J.D. Pack, *Special points for Brillouin-zone integrations.* Physical review B, 1976. **13**(12): p. 5188.
156. Vega, D. and D. Almeida, *AIM-UC: An application for QTAIM analysis.* Journal of Computational Methods in Sciences and Engineering, 2014. **14**(1-3): p. 131-136.
157. Popelier, P. and P.L.A. Popelier, *Atoms in Molecules: An Introduction*. 2000: Prentice Hall.
158. Bader, R.F.W. and R.F. Bader, *Atoms in Molecules: A Quantum Theory*. 1990: Clarendon Press.
159. Boyd, R.J. and C.F. Matta, *The Quantum Theory of Atoms in Molecules: From Solid State to DNA and Drug Design*. 2007: Wiley-VCH.
160. Lerf, A., et al., *Structure of graphite oxide revisited.* The Journal of Physical Chemistry B, 1998. **102**(23): p. 4477-4482.